



**Investigating the Morphological Transitions in an  
Associative Surfactant Ternary System**

Journal:	<i>Soft Matter</i>
Manuscript ID	SM-ART-11-2021-001668.R2
Article Type:	Paper
Date Submitted by the Author:	04-Mar-2022
Complete List of Authors:	Honaryar, Houman; University of Missouri Kansas City, Civil and Mechanical Engineering LaNasa, Jacob; The Pennsylvania State University, Department of Materials Science & Engineering Hickey, Robert; Pennsylvania State University, Materials Science and Engineering; Pennsylvania State University Shillcock, Julian; Ecole polytechnique federale de Lausanne, EPFL BMI SV LMNN Niroobakhsh, Zahra; University of Missouri Kansas City,

Cite this: DOI: 00.0000/xxxxxxxxxx

# Investigating the Morphological Transitions in an Associative Surfactant Ternary System<sup>†</sup>

Houman Honaryar,<sup>a</sup> Jacob A. LaNasa,<sup>b</sup> Robert J. Hickey,<sup>b,c</sup> Julian C. Shillcock,<sup>d,e</sup> and Zahra Niroobakhsh<sup>\*a</sup>

Received Date

Accepted Date

DOI: 00.0000/xxxxxxxxxx

Associative surfactants systems involving polar oils have recently been shown to stabilize immiscible liquids by forming nanostructures at the liquid interface and have been used to print soft materials. Although these associating surfactant systems show great promise for creating nanostructured soft materials, a fundamental understanding of the self-assembly process is still unknown. In this study, a ternary phase diagram for a system of cationic surfactant cetylpyridinium chloride monohydrate (CPCI), a polar oil (oleic acid), and water is established using experiment and simulation, to study the equilibrium phase behavior. A combination of visual inspection, small-angle X-ray scattering (SAXS), and rheological measurements was employed to establish the phase behavior and properties of the self-assembled materials. Dissipative particle dynamics (DPD) is used to simulate the formation of the morphologies in this system and support the experimental results. The ternary phase diagram obtained from the simulations agrees with the experimental results, indicating the robustness of the computational simulation as a supplement to the mesoscale experimental systems. We observe that morphological transitions (e.g., micelle-to-bilayer and vesicle-to-lamellar) are in agreement between experiments and simulations across the ternary diagram. DPD simulations correctly predict that associative surfactant systems form new nanoscale phases due to the co-assembly of the components. The established ternary phase diagram and the DPD model pave the way towards predicting and controlling the formation of different mesostructures like lamellar or vesicles, opening new avenues to tailor and synthesize desired morphologies for applications related to liquid-in-liquid 3D printing.

## Introduction

Self-assembly of amphiphilic molecules is an important tool to design a wide variety of complex nano- and mesoscale structures such as micellar, lamellar, vesicular, or other liquid crystalline phases.<sup>1,2</sup> Numerous studies on amphiphiles are concerned with ternary systems involving amphiphilic molecules (e.g., surfactants<sup>3,4</sup> or amphiphilic block copolymers<sup>5–7</sup>) and two immiscible liquids and have been of interest in applications such as pharmaceuticals,<sup>8–10</sup> oil recovery,<sup>11–13</sup> detergents,<sup>4,14,15</sup>

and synthesis of nanoporous materials.<sup>16,17</sup> For understanding and/or controlling the microstructure of these heterogeneous systems, studying the underlying equilibrium phase diagram is the most crucial step.<sup>18,19</sup> The associative surfactant-oil-water ternary systems, in particular, have intricate phase diagrams that exhibit similar but also different nanoscale morphologies to non-associative systems. However, despite the extensive work on surfactant-oil-water ternary systems, there are limited studies on surfactant ternary systems where the constituent oil headgroup possesses polarity such as fatty acids or fatty alcohols,<sup>20–23</sup> giving them dual properties as an oil (due to long alkyl chain) and a co-surfactant (due to carboxylic acid or hydroxyl function).<sup>24</sup> The interesting systems of surfactant-fatty acid-water have opened up new routes for applications in biotechnology,<sup>25,26</sup> proton conductors,<sup>24,27</sup> and liquid-in-liquid 3D printing.<sup>28,29</sup> Particularly, for the printing application, although the resulting nanoscale phases are known to exist and have enabled the printing of such materials,<sup>28</sup> the phase behavior of the used associative surfactant system is not well understood. In addition, fatty acids and their derivatives

<sup>a</sup> Department of Civil & Mechanical Engineering, University of Missouri-Kansas City, Kansas City, Missouri 64110, USA.

E-mail: niroobakhshz@umkc.edu

<sup>b</sup> Department of Materials Science & Engineering Pennsylvania State University, University Park, Pennsylvania 16802, USA.

<sup>c</sup> Materials Research Institute Pennsylvania State University, University Park, Pennsylvania 16802, USA.

<sup>d</sup> Laboratory of Molecular and Chemical Biology of Neurodegeneration, École polytechnique fédérale de Lausanne (EPFL), CH-1015 Lausanne, Switzerland.

<sup>e</sup> Blue Brain Project, École polytechnique fédérale de Lausanne (EPFL), Campus Biotech, Geneva 1202, Switzerland.

<sup>†</sup> Electronic Supplementary Information (ESI) available.

as green surface-active molecules have received increased attention due to their natural abundance, low toxicity, and biocompatibility.<sup>30,31</sup> As an example for such ternary surfactant systems with fatty acids, Noirjean et al. characterized the structural properties of the cetyltrimethylammonium bromide (CTAB)-myristic acid-water ternary system at 60 °C, above the melting point of myristic acid.<sup>24,32</sup> They provided a partial phase diagram at the low surfactant content, evidencing typical features of microemulsion systems (such as two- or three-phasic phase separation along with lamellar and reverse hexagonal phases).<sup>24,32</sup> In another category of surfactant systems with fatty acids as the oil component, the cationic surfactant is used in its hydroxide form (such as tetradecyltrimethylammonium hydroxide, TTAOH).<sup>20,21,33–35</sup> These systems are referred to as salt-free fatty acid catanionic system.<sup>20,21,33–35</sup> For such systems, formation of various structures such as uni- and multilamellar vesicle phase<sup>33,35</sup> and nanodiscs<sup>21</sup> were reported and their phase behavior,<sup>20,34,35</sup> rheological,<sup>20,34,35</sup> and structural properties<sup>33</sup> were characterized, but within a limited region of the phase diagram. Therefore, a comprehensive experimental study on the phase behavior, structural, and rheological properties of a model ternary system with a liquid fatty acid as the polar oil and a cationic surfactant in regular form has not been studied thus far. Such study is necessary for both fundamental research and further broadening the potential application of surfactant-polar oil-water systems.

Considering the promise of associating surfactant systems in creating nanostructured materials, another uncertainty about these systems which needs to be resolved is regarding the self-assembly mechanism and structural phase transitions that occur across their ternary diagrams. To achieve a clear knowledge of these aspects, especially in the early stages of self-assembly, experimental setups are limiting, mostly in terms of length and time scales.<sup>36</sup> Computer simulations with various techniques (from atomistic simulations to mean-field approaches) have proved to be helpful (either as a supplement for the theories and experiments or on their own) to model formation of nano- to mesoscale structures made from surfactants.<sup>37,38</sup> However, a careful choice of simulation technique is crucial since each approach has its own advantages and limitations, e.g., for microscopic techniques like molecular dynamics, time and length scales are limited to small system sizes and short times while mean-field approaches lead to the loss of critical details.<sup>39</sup> Mesoscopic simulations such as dissipative particle dynamics (DPD) as an alternative intermediary method have made it possible to investigate the mesostructure of complex fluids and amphiphile systems on time and length scales that are otherwise unreachable from microscopic simulations with adequate degree of molecular details.<sup>37,39–42</sup> DPD simulations have been successfully used for modeling various complex fluids such as lipid bilayers and cell membranes,<sup>43,44</sup> surfactants,<sup>37,45</sup> polymers,<sup>46,47</sup> and colloidal suspensions.<sup>48</sup> In particular and to our interest, DPD has proved to be a powerful tool for investigating morphological transitions in ternary systems.<sup>49,50</sup> However, no studies to date, have established a simulation model which is verified experimentally and can successfully predict the

phase behavior representative of a ternary system comprising a cationic surfactant, a long-chain polar oil, and water.

Here, we report the detailed phase behavior and rheological properties of a ternary system comprised of cationic cetylpyridinium chloride monohydrate (CPCl), a polar oil (oleic acid, OA), and water using visual inspection, small-angle X-ray scattering (SAXS), and rheological measurements. Across the phase diagram, the system exhibits a rich phase behavior induced by co-assembly of the components and four distinct regions are identified; micellar ( $L_1$ ), lamellar/vesicle ( $L_\alpha$ ),  $L_1/L_\alpha$  biphasic, and phase separated. Accordingly, rheological properties of the system vary across the diagram where the  $L_1$  region shows Newtonian behavior (constant, rather low viscosity) and  $L_\alpha$  exhibits gel-like behavior with shear-thinning properties. Rheological characteristics of  $L_1/L_\alpha$  biphasic samples indicate that the top layer is comprised of mostly  $L_\alpha$  phase in the presence of  $L_1$  while the bottom phase is  $L_1$  with small amounts of bilayer or other intermediate structures. Then using the coarse-grained DPD simulation tool, a model is proposed and validated by the self-assembly behavior of the binary systems of each component (CPCl and OA) in water, and is used to study the system morphologies. The ternary phase diagram obtained from simulations is also compared with the experimentally established results, and shows a significant similarity, specifically in terms of morphological transitions observed with a change in concentration of one component. The DPD simulation model presented here is validated by experimental results and is very well suited to study the intricate phase behavior of the same type of the associative surfactant systems (*i.e.*, surfactant-polar oil or alcohol-water).

## Experimental and method

### Materials

Oleic acid (OA, technical grade 90%) was obtained from Alfa Aesar. Cetylpyridinium chloride monohydrate (CPCl, 99.0–102.0%) and Nile red were purchased from Sigma-Aldrich. All chemicals were used as received without further purification. Purified, deionized water was used for preparing samples.

### Sample preparation

The isothermal phase diagram for the reported system was mapped out by preparing over 50 samples at different CPCl, oleic acid, and water weight percents. Due to the solubility limit of CPCl surfactant in water ( $\approx 33$  wt%),<sup>51</sup> the focus of this study is on water-rich corner of the ternary phase diagram (water  $\geq 70$  wt%). To prepare samples for SAXS characterization and rheological measurements, the CPCl surfactant is dissolved in deionized water at different concentrations (up to 560 mM) and oleic acid is added the next day. In many samples, OA was found to stay phase separated during the mixing step. To help dissolve the insoluble OA fraction, samples were shaken and/or stirred for several days at elevated temperatures of 40–80 °C, which is common in similar ternary systems.<sup>20,24,32,33,35,52</sup> Specifically, mixtures were heated to 77 °C for 2 h in an oven (Shel Lab, VWR), and then the mixture was stirred manually and placed in a

sonication bath (Aquasonic, VWR Scientific) for 1 h a day. These heating and mixing steps were repeated for five days until the sample did not contain any trace of insoluble materials.

### Small-angle X-ray scattering (SAXS)

The day after preparation of samples, small-angle X-ray scattering (SAXS) experiments were carried out on samples by employing an in-house SAXS/WAXS laboratory beamline (Xeuss 2.0 HR, Xenocs, France) using a 2D X-ray detector (Pilatus 200K, Dectris) and microfocus sealed tube (copper) as a beam source with X-ray wavelength of 1.54 Å and the beam size of 0.6 mm × 0.5 mm. The beamline was configured with an approximately 2.5 m sample-to-detector distance. Samples were contained in a 1.5 mm nominal diameter quartz capillary (0.01 mm wall thickness, Charles Supper Company) and scattering experiments were carried out at room temperature ( $\approx 22$  °C). For sample preparation, the sample was first rigorously mixed using a vortex mixture (analog, Fisher Scientific), then a small amount of the mixture was pulled with a syringe and filled in the capillary. Finally, it was centrifuged down and sealed. Prior to measurements, capillaries were sealed with epoxy and cured overnight to settle down. The prepared samples in capillaries showed similar phase domains as in the original container. For bulk samples, the measurements were repeated for several vertical positions to ascertain the homogeneity of the bulk samples and the consistency of the scattering data. Samples with more than one phase were characterized by shifting the vertical position of the sample stage and recentering the beam on the capillary. The 2D isotropic scattering intensities were integrated and 1D plots of scattered intensity,  $I(q)$ , is obtained in arbitrary units (a.u.) versus scattering wave vector  $q = 4\pi\sin(\theta/2)\lambda^{-1}$ , where  $\theta$  is the scattering angle and  $\lambda$  is the beam wavelength. The scattering profiles were then shifted on a log  $I$  scale for better visualization.

### Rheological measurements

Using a stress-controlled Discovery-HR3 rheometer (TA Instruments), continuous and oscillatory shear rheometry were performed at a controlled temperature of  $25 \pm 0.5$  °C. Geometry that has been used was either 40 mm-diameter parallel plate or concentric cylinder depending on sample behavior and its characteristics. The concentric cylinder geometry is used for testing samples with low viscosity that are pourable into the cup. This geometry consists of a steel outer cylindrical cup and a titanium inner rotor (DIN conical rotor). The cup sits in a temperature-controlled Peltier jacket, which is mounted on the rheometer. Parallel plate geometry is used for gel-like samples which were carefully loaded onto the lower plate to minimize shearing effects and allowed to rest for about 10 min prior to measurement and the gap was set at 500  $\mu\text{m}$  for all tests. For the gel-like samples, the concentric cylinder geometry is not used since with this geometry, the sample is loaded into a cup, and hence it is impossible to see or remove the air bubbles which form and get entrapped within the sample during loading. Also, the cone and plate geometry is not used since this geometry is designed to operate only at the extremely low truncation gap

of 51  $\mu\text{m}$  (for the 2° angle cone and plate geometry) and for reaching such a small gap, high axial stresses will be applied on the sample which might affect the structures in the samples. For the gel-like samples, the rheological tests are repeated with roughened surface geometries (*i.e.*, 40 mm-diameter parallel plate geometry with sand-blasted surfaces) if the results are suspected to be influenced by wall slip effect. The slip wall effect is a common problem when testing highly concentrated samples and is usually caused due to velocity gradients which happen to be large in a thin region adjacent to the geometry wall.<sup>53,54</sup>

Amplitude sweeps (oscillatory strain sweeps) were performed at a constant angular frequency ( $\omega$ ) of 1 rad  $\text{s}^{-1}$  over a shear strain range of 0.01% to 100% to determine the linear viscoelastic region (LVR). Oscillatory frequency sweeps were then carried out over a frequency range of 0.1 to 100 rad  $\text{s}^{-1}$  at a constant strain amplitude of 1% which is within the LVR of all gel samples as evidenced by the oscillatory strain sweep profiles. Viscoelastic parameters, *i.e.*, storage modulus ( $G'$ ) and loss modulus ( $G''$ ) were obtained from frequency sweep experiments. For oscillatory shear rheometry, the data affected by instrument inertia, mostly at high frequencies values are omitted. Per rheometer manufacturer's instruction, these data are diagnosed by looking at the raw phase difference between the oscillating displacement and torque signals where values higher than 175° are considered instrument inertia artifacts. Furthermore, data obtained with a torque close to the limit of instrument (lower than 1  $\mu\text{N m}$ ) were not reported. For all samples, each oscillatory test was repeated three times to ensure consistency of data. The flow sweep test with steady-state sensing was performed to characterize the flow behavior of samples with an increasing shear rate from 0.001  $\text{s}^{-1}$  to 100  $\text{s}^{-1}$ . With the steady-state sensing, the samples were subjected to the desired shear rate for a sufficiently long time to achieve a steady-state, which in turn maximizes the reliability of data.

### Confocal and fluorescence microscopy

Samples were imaged using a confocal microscope (TCS SP8, Leica Microsystems, UK) and a fluorescence microscope (Axio Lab.A1, Zeiss). To prepare samples for fluorescence microscopy, Nile red was added to OA at the concentration of 0.01 mg  $\text{mL}^{-1}$  during sample preparation.

### Simulation method

For the dissipative particle dynamics (DPD) simulations performed here, we use the open-source polymer research engine - dissipative particle dynamics (Osprey-DPD) which can be found on Github.<sup>55</sup> In the DPD technique, molecules are composed of beads that represent small volumes of atoms or molecular groups that interact via soft, short-ranged forces. The molecular architecture, concentration, and force field are specified and the simulation is evolved by integrating Newton's laws of motion for all constituent beads. The reader is referred to the literature for more details of the DPD method<sup>39</sup> and for an in-depth review.<sup>37,56</sup> The total force acting on a particular bead is the sum of a conservative force ( $F_{ij}^C$ ), a dissipative force ( $F_{ij}^D$ ), and a

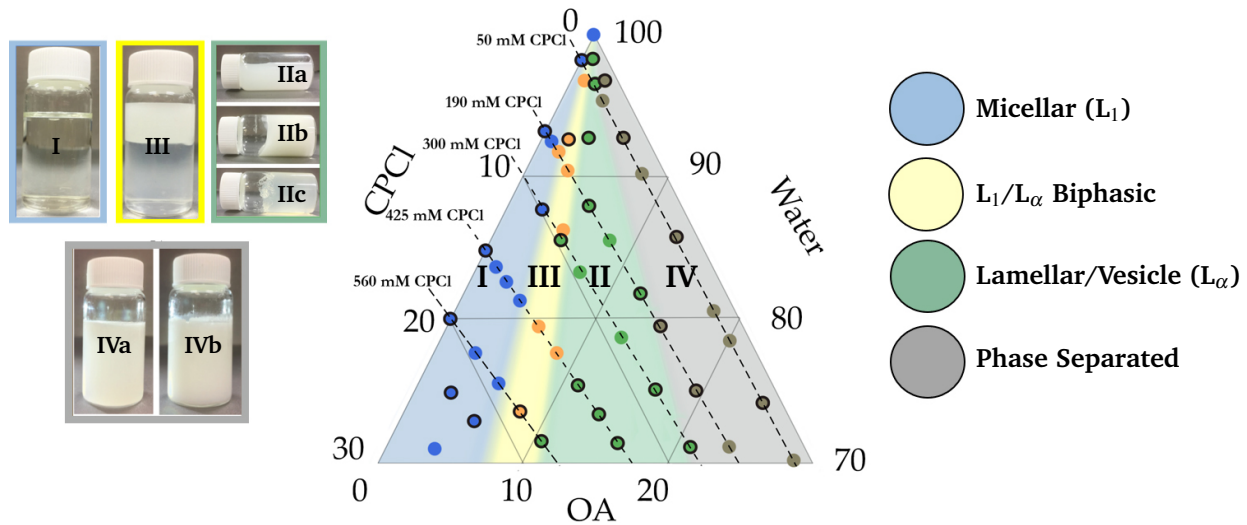


**Fig. 1** Water-rich corner of the ternary phase diagram for CPCI-OA-water obtained using SAXS and visual inspection. The compositions in the ternary phase diagram are expressed in terms of weight percent. Prepared samples are shown as circles on the ternary phase diagram, and outlined circles represent samples that have been characterized using SAXS. Four regions are identified and discussed separately and the typical samples for each region are shown on the left. The dashed lines are drawn to indicate the compositions with a constant concentration of CPCI. By moving along these lines from left to right, OA content increases while the surfactant concentration remains unchanged (constant  $\text{wt}\%_{\text{CPCI}}/\text{wt}\%_{\text{water}}$ ).

random force ( $F_{ij}^R$ ). The conservative forces between  $i$  and  $j$  beads for  $r_{ij} \leq d_0$  (where  $d_0$  defines the length scale in the simulations) is as follows:

$$F_{ij}^C = a_{ij}(1 - r_{ij}/d_0)\hat{r}_{ij}, \quad (1)$$

where  $a_{ij}$  is the maximum force,  $r_{ij} = r_i - r_j$  is the relative position vector from bead  $j$  to bead  $i$  ( $r_{ij}$  as its magnitude), and  $\hat{r}_{ij}$  is the unit vector directed from bead  $j$  to bead  $i$ . DPD conservative interaction parameters,  $a_{ij}$ , represent the chemical identity of beads and interactions at the mesoscopic level such as van der Waals, screened electrostatic, hydrophobicity, and hydrogen bonding.

The other two nonbonded forces, the dissipative and random forces, are given by Equations 2 and 3, respectively. These forces constitute a thermostat to ensure that the equilibrium states of the simulation are Boltzmann distributed.<sup>39</sup>

$$F_{ij}^D = -\gamma_{ij}(1 - r_{ij}/d_0)^2(\hat{r}_{ij} \cdot v_{ij})\hat{r}_{ij}, \quad (2)$$

$$F_{ij}^R = \sqrt{2\gamma_{ij}k_B T/dt}(1 - r_{ij}/d_0)\xi_{ij}\hat{r}_{ij}, \quad (3)$$

where  $\gamma_{ij}$  is the strength of the dissipative force,  $v_{ij}$  is the relative velocity between beads  $i$  and  $j$ ,  $k_B T$  is the system temperature.  $\xi_{ij}$  is a symmetric, uniform, unit random variable that is sampled for each pair of interacting beads and satisfies  $\xi_{ij} = \xi_{ji}$ ,  $\langle \xi_{ij} \rangle = 0$ , and  $\langle \xi_{ij}(t)\xi_{kl}(t') \rangle = (\delta_{ik}\delta_{jl} + \delta_{il}\delta_{jk})\delta(t - t')$ . The pairwise forms of the dissipative and random forces conserve momentum. The factor  $1/\sqrt{dt}$  in the random force ensures that the discretized form of the Langevin equation is well defined.

To make up the structure of each molecule in simulation, beads are connected to each other using Hookean springs with potential energy:

$$U_2(i, i+1) = (1/2)k_2(r_{i,i+1} - l_0)^2, \quad (4)$$

where  $k_2$  and  $l_0$  (in units of  $k_B T/d_0^2$  and  $d_0$ , respectively) are the spring constant and unstretched length of the bond and are chosen to be 128 and 0.5 for all bead pairs, respectively, similar to other relevant work.<sup>40,42</sup> Alkyl chain stiffness is imposed in the simulations by adding a chain bending potential to the angle  $\theta$  defined by adjacent triples of beads in the CPCI and OA:

$$U_3(i-1, i, i+1) = k_3(1 - \cos(\theta - \theta_0)), \quad (5)$$

where the stiffness parameter ( $k_3$ ) and the preferred angle ( $\theta_0$ ) are defined for each distinct set of bead triples. The bead triplet that includes the OA double bond has the parameters  $k_3=15$  and  $\theta_0=45$  degrees to represent the kink induced by the bond.<sup>40,42</sup> All other bead triples have the parameters  $k_3=15$  and  $\theta_0=0$  that keep the chains relatively straight.

The dimensions of the box in all simulations were  $L_x \times L_y \times L_z \times (d_0)^3 = (32d_0)^3$  unless otherwise told. We choose the bead density ( $\rho$ ) to be 3 based on the literature<sup>41,57</sup> which means every three beads occupy a cube with volume of  $d_0^3$  in the simulation box ( $\rho d_0^3 = 3$ ). Given the bead density, the simulation box ( $32^3 \text{ nm}^3$ ) contains 98304 beads and periodic boundary conditions were applied in all three directions. In the simulations, all length scales are measured in units of the  $d_0$ , all beads mass in units of  $m_0$ . The energy scale is set to  $k_B T = 1$  (where  $k_B$  is the Boltzmann constant and  $T$  is the temperature), which fixes the magnitude of the total bead kinetic energy and the ratio of the random and dissipative force parameters.<sup>39</sup> Therefore, the simulation time is measured in units of the DPD time scale  $\tau = \sqrt{m_0 d_0^2 / k_B T}$ . The simulation runs for 2,000,000 steps with a time step of  $0.02\tau$ . The temperature and pressure were taken as the observables to check that the system has reached equilibrium. Additionally, it has been ensured that the formed structures do not change with longer simulation time, indicating that equilibrium has

been reached and the achieved local free energy minima prevent further transformation.

For constructing a mesoscopic model, we first determine the volume of the simulation beads and then determine the length scale. Three to four carbon atoms with an equivalent volume of  $120 \text{ \AA}^3$  are taken together<sup>58</sup> and grouped into one bead, and thus each bead represents liquid volume of  $120 \text{ \AA}^3$ . Given a water molecule volume of  $30 \text{ \AA}^3$ ,<sup>57</sup> each water bead ("W") represents four water molecules. In other words, the real-space renormalization factor ( $N_m$ ) is set to 4 which is defined as the number of water molecules that each bead represents as proposed by Groot and Rabone.<sup>57</sup> As we chose the bead density equal to  $\rho d_0^3 = 3$ , a  $d_0^3$  cube should contain three beads, and therefore a volume of  $360 \text{ \AA}^3$ . The length scale ( $d_0$ ) then can be calculated as:<sup>57</sup>

$$d_0 = (360)^{1/3} \text{ \AA} = 7.11 \text{ \AA} \quad (6)$$

This length mapping gives us a length of around 22 nm ( $= 32 \times d_0$ ) for each axis of the simulation box.

A simulation is started by creating the appropriate number of molecules of each component that correspond to a specific composition in the phase diagram, and randomly distributing them throughout the simulation box. The simulation is allowed to evolve to an equilibrium morphology that minimizes the free energy of the system. Configurations generated by the simulations are visualized with ParaView software<sup>59</sup> and the structure of the system was determined by visual inspection after equilibrium was reached. For each system, we assign a relevant time scale to the simulation by comparing the dimensionless diffusion constants with experimental values (explained in Result and discussion section).

### System size dependence study in simulation

The simulation box with a linear size of  $32d_0$  is initially used for the DPD simulation of all studied compositions since it is of reasonable size with respect to formed structures and computationally affordable. However, this simulation box size in some cases may fail to capture the true equilibrated structures or their features. Furthermore, a small simulation box might even force aggregates into a shape that is at the lowest free energy given that they are connected across the box, but may not be the actual equilibrium state in a larger box. Therefore, to address these concerns, a system size dependence analysis is carried out where the compositions with structures that are speculated to be affected by simulation box size are simulated again, but in a larger simulation box with the linear size of  $64d_0$ , which is eight times larger than the initial simulation box.

## Results and discussion

### Experimental results

Based on visual inspection and SAXS measurements, all the samples exhibit morphologies that reside in four distinct regions of the ternary phase diagram; micellar ( $L_1$ ), lamellar/vesicle ( $L_\alpha$ ),  $L_1/L_\alpha$  biphasic, and phase separated. All the prepared mixtures and the assigned regions along with typical samples for each region are shown in Figure 1, where the outlined data

points represent the samples, for which SAXS measurements were performed. It is worth mentioning that the ternary diagrams in this work are rotated and inverted such that the top vertex of the triangle represents the point of 100% of the solvent (water) for easier discussion. Typical SAXS patterns of samples and their rheological properties are shown in Figure 2 and Figure 3, respectively, and will be discussed in detail for each region in the following sections.

### I. Micellar region ( $L_1$ )

In the micellar region (shown in light blue in Figure 1), the obtained solutions are low-viscous and water-like (vial "I", Figure 1) similar to pure CPCl solutions. This behavior implies that small amount of oleic acid molecules (up to 5.6 wt% for 560 mM CPCl solution) are dissolved in the solutions in this region. The scattering patterns of the samples in this region shows similarity to those of pure CPCl solutions (Figure 2a). The pure CPCl is known to self-assemble into spherical or ellipsoidal micelles in water.<sup>29,60,61</sup> Overall, the mean micelle-to-micelle spacing ( $D = 2\pi/q^*$ , where  $q^*$  is the position of correlation peak) decreases with increasing OA content (colored patterns in Figure 2a). Similar decreases in micelle-to-micelle spacing are seen for pure CPCl solutions with increasing CPCl concentration (black patterns in Figure 2a). However, these micelle-to-micelle distances for the samples in this region proved to be larger compared to that of the pure surfactant solutions, suggesting that OA molecules either enter into the micelle core or co-assemble with CPCl to become larger (forming swollen micelles) and accommodate more CPCl and OA molecules in a micelle.

Rheological properties of three samples (labeled as "M1-M3" in the diagram of Figure 3a) are studied at fixed CPCl concentration of 425 mM and increasing OA concentration. The concentric cylinder geometry is used for these samples because of their very low viscosity. The plot in Figure 3a shows the viscosity as a function of shear rate obtained from steady shear experiments for these samples. The viscosity of solutions increases from  $\eta = 2.8 \pm 0.08 \text{ mPa s}$  to  $\eta = 4.74 \pm 0.25 \text{ mPa s}$  with a decrease in the water content and an increase in OA (from "M1" to "M3"). This increase in viscosity, however, is not significant which suggests that the swollen micelles remain short in this region and are unlikely to transform into long worm-like micelles. Frequency sweep results for samples in the micellar region (I) could not be obtained due to large instrument inertia contributions (see Experimental and method section).

### II. Lamellar/vesicle region ( $L_\alpha$ )

The lamellar/vesicle region (shown in green in Figure 1) resides around the equimolar line of OA and CPCl, and the obtained solutions were one phase. At the top corner of this region, the solutions appear to be low-viscous but turbid (vial "IIa" in Figure 1) and as we move to lower water content, the solutions become thicker and gel-like but showed to be rather semitransparent (vial "IIc" in Figure 1). At the right side of the equimolar line, where the content of OA is higher (12 wt% OA for 190 mM CPCl), a thick milk-like phase forms (vial "IIb" in Figure 1). In the region II, all the samples show peaks at

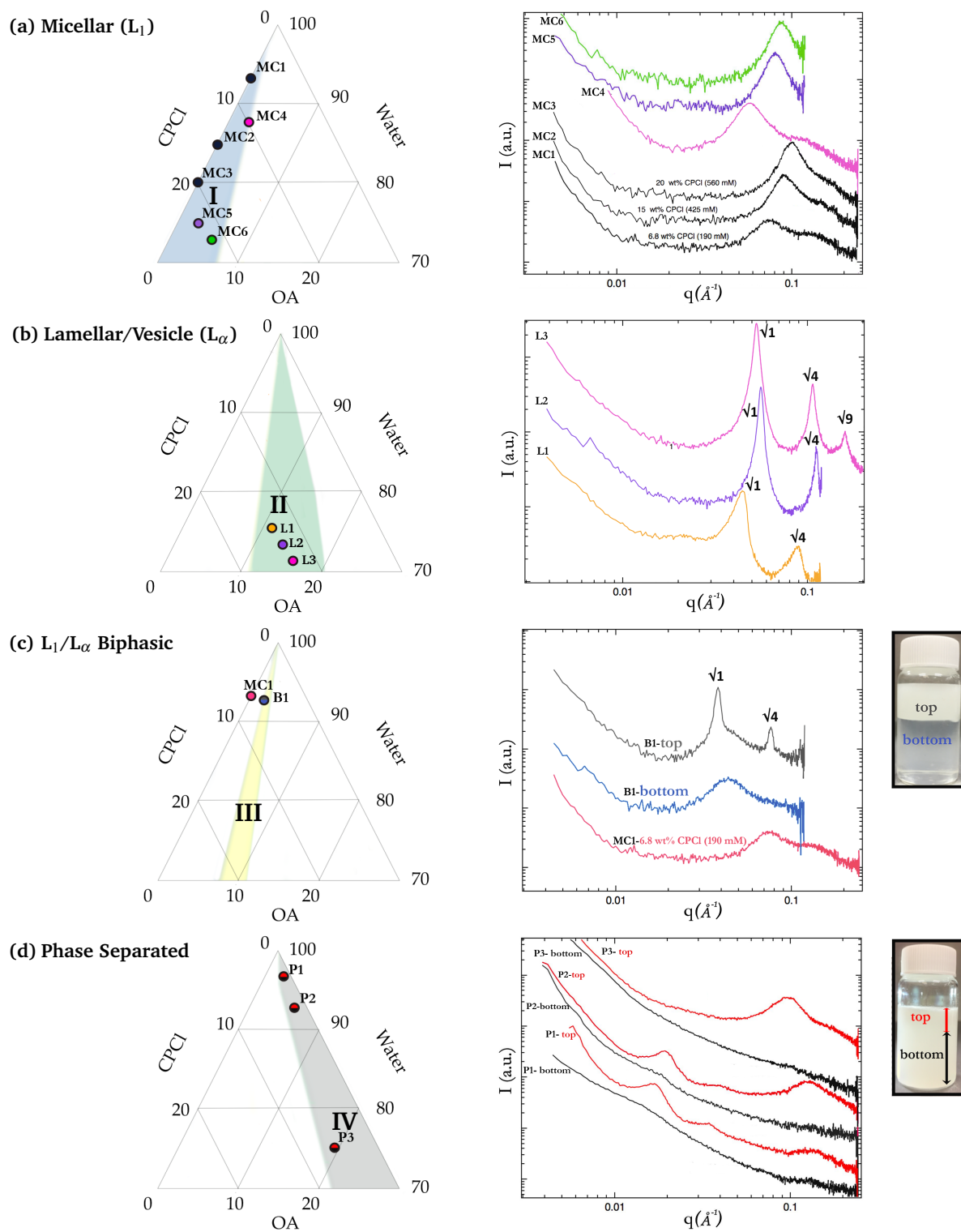


**Fig. 2** Representative SAXS patterns of samples in each region: (a) Scattering patterns and location of three points in the micellar region I (colored) and pure surfactants (black). (b) Location of three points on the constant CPCI concentration line in the lamellar/vesicle region (II) of the ternary phase diagram along with corresponding scattering patterns. (c) Comparison between scattering patterns of a pure CPCI solution and a  $L_1/L_\alpha$  biphasic sample in the region III. (d) Location of three samples ("P1-P3") in the phase separated region (IV) of the ternary phase diagram and the corresponding scattering patterns. The compositions in the ternary phase diagram are expressed in terms of weight percent.

$q^*$  and  $2q^*$ , (and  $3q^*$ ) where  $q^*$  is the first reflection in their SAXS patterns (Figure 2b). These SAXS patterns suggest the presence of  $L_\alpha$  phase, *i.e.*, densely packed uni- and multilamellar

vesicles or lamellar phases<sup>20,34</sup> or a mixture of two.<sup>62</sup> It is not possible to assign this  $L_\alpha$  phase to one structure or the other using SAXS patterns alone. Furthermore, the method of

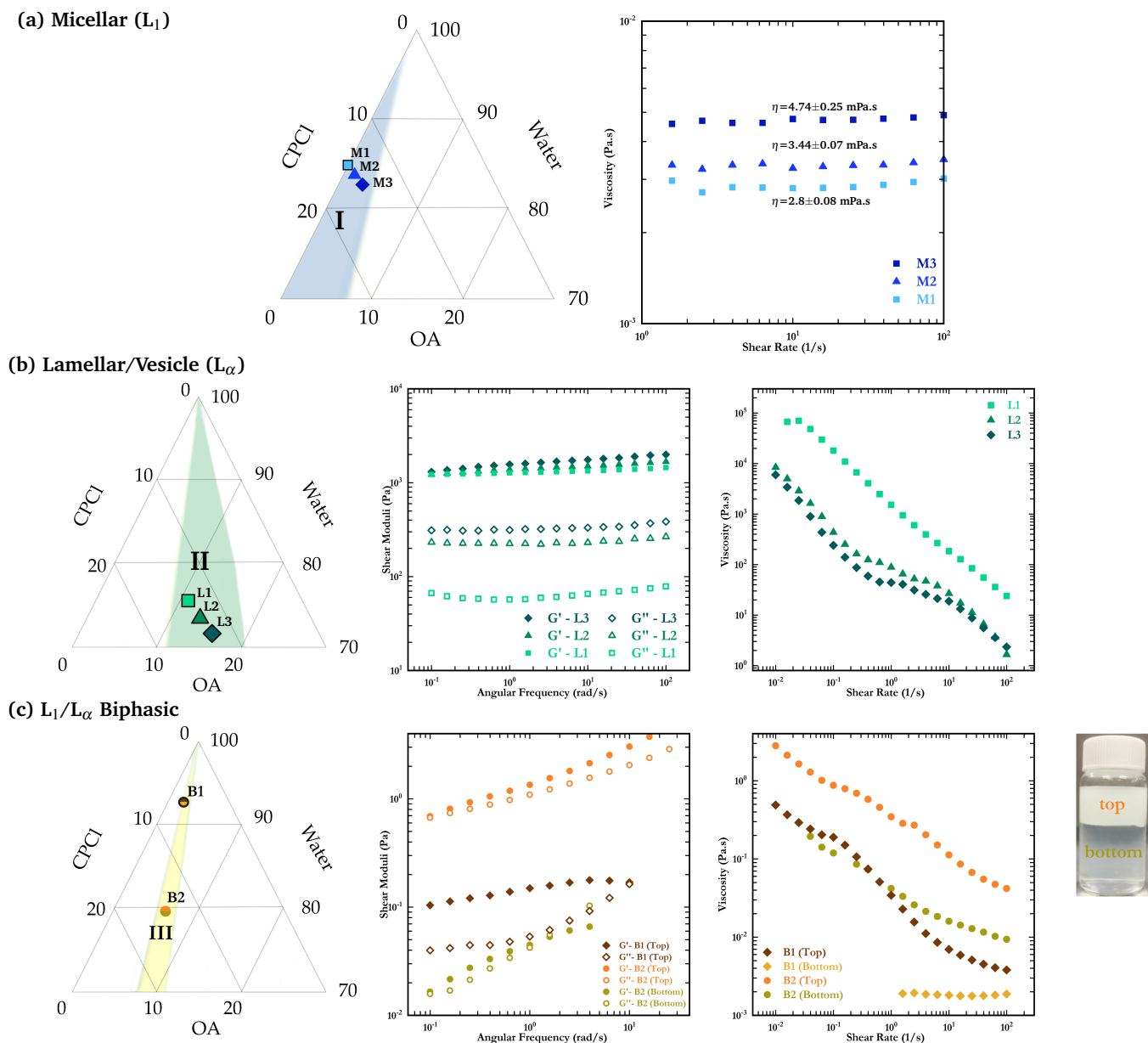


**Fig. 3** Rheological characterization of samples along with their locations in the phase diagram for  $L_1$  (a),  $L_\alpha$  (b), and  $L_1/L_\alpha$  biphasic (c) regions. The compositions in the ternary phase diagram are expressed in terms of weight percent. Shear moduli as the function of angular frequency ( $\omega$ ) is obtained at a fixed strain of 1% which is within the LVR region (Figure S1, ESI<sup>†</sup>). For viscosity versus shear rate curves, the data points that were acquired without meeting steady-state condition are not reported. Frequency sweep results for the bottom phase of sample "B1" (in the biphasic region) and samples in the micellar region (I) could not be obtained since the data were affected by instrument inertia (see Experimental and method section).

mixing during the preparation of samples can complicate such a decision as applying even small shearing forces during sample preparation can transform the lamellar phase into vesicles.<sup>63</sup> Nevertheless, all of these structures are comprised of OA/CPCI bilayers alternating between layers of water. Based on SAXS results, the interlayer spacing for all measured samples across this region ( $D = 2\pi/q^*$ ) falls between  $\approx 12$  nm and  $\approx 29$  nm. We have observed an increase in the interlayer spacing of lamellar/vesicle structures from 11 nm to 22 nm when we increase the water content significantly from  $\approx 71$  wt% to  $\approx 82$  wt% on a constant  $\text{wt}\%_{\text{OA}}/\text{wt}\%_{\text{water}}$  line (Figure S2b, ESI<sup>†</sup>),

whereas for two samples with the constant water content of  $\approx 71$  wt%, the interlayer size remains unchanged (Figure S2c, ESI<sup>†</sup>). These observations are expected as the thickness of the CPCI/OA bilayer can be considered almost constant (equals twice the length of the hydrocarbon tail of CPCI or OA,  $\approx 4$  nm) and change in water content should determine the domain spacing.

The viscoelasticity and flow behavior of the system in the lamellar/vesicle region (II) is studied along the constant 425 mM CPCI concentration line and for the same compositions labeled as "L1-L3" in Figure 2b diagram. For these samples, the parallel plate geometry was used since they exhibited the gel-like behavior (as

discussed in Experimental and method section). Based on the frequency sweep results, the storage modulus ( $G'$ ) is about an order of magnitude larger than the loss modulus ( $G''$ ). Both shear moduli are almost independent of angular frequency (a typical behavior for a viscoelastic gel)<sup>64,65</sup> considering only 0.1 decade increase in moduli over three orders of magnitude increase in angular frequency.

The viscosity-shear rate curves for these samples are shown in the right-hand plot of Figure 3b which are found to change only slightly against a rise in OA content. All the samples show shear-thinning behavior with four orders of magnitude decrease in viscosity over the measured shear rate range. With increasing OA concentration (from "L1" to "L2" and "L3") the viscosity-shear rate curve drops but starts adopting a shoulder at medium shear rates, similar to what was observed for bilayer structures (densely packed vesicles) in another study.<sup>20</sup> The sharper decrease in the viscosity observed before the shoulder is most likely due to a yielding effect that is attributed to a possible shear-induced microstructural transitions (typical of a lamellar phase) and is caused once a critical stress is applied to a structured sample for a sufficient time.<sup>20,66</sup> However, to fully understand the underlying reason for the steady flow behavior of a lamellar phase, especially the shoulder part of the curve, future work will be focused on *in situ* observations of such shear-induced microstructural transitions.

### III. $L_1/L_\alpha$ biphasic region

In the  $L_1/L_\alpha$  biphasic region (shown in yellow in Figure 1) which lies between regions I and II, two phases are observed (vial "III" in Figure 1); the top layer is turbid and the layer on the bottom is a blueish water-like solution. SAXS measurements are performed on both the upper and bottom phases of the data point shown in the diagram of Figure 2c. The phase at the bottom shows a similar pattern to that of the pure CPl solution but with a shift in the correlation peak to the lower  $q$ , in agreement to what was observed for solutions in the micellar region (I). Such a shift to lower  $q$  in the scattering curve indicates further spatial separation between micelles, which could be due to the reduction in the micelle concentration of the bottom phase since a portion of the CPl molecules co-assemble with OA in the top phase. While this behavior indicates swollen micelles ( $L_1$ ), the SAXS pattern of the top phase reveals peaks at  $q/q^* = 1, 2$ , implying a bilayer phase ( $L_\alpha$ , region II). In addition to these major peaks, the SAXS pattern for the top phase exhibits a coexisting single broad peak similar to the bottom phase at the same position which suggests that there is a small amount of micellar structures within this phase. Therefore, we conclude that this region is the coexistence of structures observed in the regions I and II, which leads to the formation of two phases (biphasic, III). In fact, for this intermediate region, different aggregates that coexist in the sample (micellar and lamellar/vesicle) cause the formation of multiphase regions, similar to the aqueous biphasic regions in catanionic systems (that are made of anionic and cationic surfactants).<sup>20,33,35</sup> In these systems, the driving force for the phase separation is the difference in the density of coexisting aggregates since the density of bilayers tends to be lower than

that of micelles.<sup>20,33</sup>

For two samples within this region (labeled "B1-B2" in Figure 3c diagram), the upper and bottom phases were collected separately and rheological measurements were carried out using a concentric cylinder geometry (due to their low viscosities). Results of frequency and flow sweep tests are provided in Figure 3c for both samples. In the top phase of sample "B1",  $G'$  is higher than  $G''$ , indicative of a dominant elastic behavior with a crossover point at higher frequencies and for the bottom phase, the measurement of the moduli at higher angular frequencies were not possible due to the dominant instrument inertia, similar to micellar samples in the region I. For the sample "B2" which is on the 425 mM CPl concentration line, the top phase shows slightly higher values for  $G'$  than those of  $G''$  (with  $G'-G''$  crossover point at low frequencies) while this difference in shear moduli is more apparent for the top phase of sample "B1". For the bottom phase of sample "B2", both shear moduli show frequency dependency and exhibit a crossover point with  $G'' < G'$  in low- $\omega$  region and  $G'' > G'$  in medium- $\omega$  region. Compared to sample "B1" for which no data could be obtained due to large instrument inertia contributions, shear moduli of the bottom phase of sample "B2" could not be acquired only at higher angular frequencies.

Comparing the viscoelastic properties of samples along the 425 mM CPl concentration line in both region II and III ("B2" and "L1-L3", Figure 3b-c) illustrates that unlike samples in the vesicle/lamellar region ("L1-L3") where  $G'$  is at least one order of magnitude higher than  $G''$ , shear moduli of both top and bottom phases of sample "B2" are almost equal and display a crossover point. Furthermore, compared with samples "L1-L3" with only 0.1 decade increase in shear moduli, the frequency dependency for shear moduli is more apparent for the biphasic sample ("B2") where a significant increase for  $G'$  and  $G''$  is observed up to one order of magnitude over the measured angular frequency range. Such noticeable differences in rheological behavior are attributed to swelling of bilayer domains due to the coexistence of micellar and lamellar structures as evidenced in their SAXS responses.

In flow sweep tests (right-hand plot in Figure 3c), top phases in both samples exhibit shear-thinning behavior with almost two orders of magnitude decrease in viscosity over the measured shear rate range. The higher water content of sample "B1" leads to one order of magnitude drop in viscosity curve compared to that of "B2" top phase. Combination of rheological properties for the top phase, *i.e.*, shear-thinning behavior and frequency-dependent moduli, suggests the coexistence of both bilayers and micelles, consistent with obtained SAXS results. For the bottom phases, sample "B1" shows Newtonian behavior with a constant viscosity. Shear moduli for this phase could not be obtained over the entire frequency ranges which along with its Newtonian behavior (constant, rather low viscosity) is similar to the micellar samples in the region I and in agreement with its SAXS response. However, for the sample "B2" bottom phase, a shear-thinning behavior is observed with a viscosity one order of magnitude lower than that of the top phase at any shear rate. The shear-thinning properties and gel-like behavior of the "B2" bottom phase suggest the presence of bilayers or other intermediate structures in this phase, but possibly in small amounts that were

not captured in SAXS measurements.

#### IV. Phase separated region

In the phase separated region (shown in grey in Figure 1), a water-oil phase separation takes place between oleic acid and water, similar to microemulsion systems.<sup>1,67</sup> For samples in this region, two phases were observed with the upper phase looking like semitransparent or turbid solutions while the lower phase is a white-milk solution (vials "IVa" and "IVb", Figure 1). For samples in region IV, assigning a discrete phase boundary between the upper and lower layers was difficult as opposed to the biphasic region (III) as shown in Figure 1. However, once the oleic acid is stained with fluorescent Nile red, distinguishable colors were identified for the top and bottom phases (Figure 4a), suggesting that the top phase (pink-colored) is oil-rich, and the bottom phase (white-colored) is water-rich. These results are confirmed by the fluorescence microscopy images (Figure 4b-d), where the top phase consists of a bright continuous oil region with dark water droplets with a range of diameters, reaching up to several hundred micrometers (Figure 4c). In contrast, the continuous phase for the bottom phase (Figure 4d) is dark with oil droplets appeared as bright. Thus, in the region IV, the top and bottom phases are classified as water-in-oil and oil-in-water emulsions, respectively. The formation of such two emulsion phases is typical of generic surfactant-oil-water systems.<sup>1</sup>

SAXS measurements were also carried out on upper and lower phases for samples in the region IV to determine if nanostructures were also present in the emulsions (Figure 2d). Specifically, for the upper phase, samples "P1-P3" exhibit a broad peak at  $q \approx 0.1 \text{ \AA}^{-1}$  that resembles the structure factor of a spherical phase. As the water content is increased from "P3" to "P1", lower- $q$  scattering features that index to a lamellar phase emerge, in addition to a broad peak at high- $q$  values, suggesting a coexistence of multi-lamellar vesicles and a spherical phase. It is worth noting that the length scales probed through SAXS are nanometer scale, and micron-scale features of emulsion phases are only quantified from the fluorescence micrographs. The emulsion dimensions on the order of ones to tens of micrometers is typical of spontaneously formed emulsions.<sup>68</sup> Thus, the emulsions in the upper water-in-oil are predicted to consist of complex droplets with internal lamellar and spherical nanostructures.

The lower oil-in-water phase for samples in the region IV on the other hand has subtle scattering features consisting of a single broad peak. The broad peaks are at  $q \approx 0.014$  and  $0.018 \text{ \AA}^{-1}$  for samples "P1" and "P2", respectively. Although there is a possibility that a low concentration of oil droplets has internal nanostructures similar to the upper water-in-oil phases, the lack of features in the SAXS patterns suggests that the oil droplets are more similar to traditional oil-in-water emulsions. The fluorescence micrographs also support that the oil droplets in the lower oil-in-water phase exhibit more homogeneous fluorescence as compared to the water droplets in the upper water-in-oil phase.

#### Simulation results

The first step in simulations is to determine the representation of each molecule type (*i.e.*, the architecture of molecules). There have been simulation studies on ternary phase behavior of systems composed of surfactant-oil-water<sup>38,58,69,70</sup> where the oil components are composed of a chain of hydrophobic beads, but there has not been much focus on systems where the oil is polar and has surface activity. For amphiphilic systems, molecules have been mostly represented as simple models such as dimers composed of a hydrophilic head and a hydrophobic tail.<sup>70</sup> Here a more precise representation of amphiphiles, *i.e.*, CPCl surfactant and oleic acid molecules, are used with seven beads. The molecules are shown in Figure 5, together with their mapping onto the coarse-grained DPD model. Following another work where the headgroup of ionic surfactants is represented with two beads,<sup>58</sup> the headgroup of CPCl is represented here with two bead types, "N" and "M", where "M" type bead represents the repulsion arising from the bulky, charged pyridinium group, while "N" captures the hydrophilicity of the overall headgroup. A "C1" bead type is distinguished from other "C" type beads in order to include bending stiffness for representation of OA double bond in the simulation. This mapping yields a linear architecture of  $\text{MNC}_5$  for CPCl molecules and  $\text{HC}_2\text{C1C}_3$  for OA molecules (Figure 5). With this representation, both OA and CPCl molecules will have the same length in simulation with seven beads. Although CPCl surfactant has 16 carbon atoms in its hydrophobic tail and OA molecule has  $n = 18$  carbons in the hydrocarbon chain, the *cis*-double bond of the OA makes it slightly shorter in length than a saturated chain,<sup>71</sup> which justifies the assumption of same length for OA and CPCl molecules. The solvent water is represented by a single bead "W", with each "W" bead representing four water molecules (see Experimental and method section).

The second step in our simulation technique is to correlate the conservative interaction parameters with the self-assembly behavior of both pure surfactant (CPCl) in water and oleic acid (OA) in water so that they are well represented in the simulations of the ternary phase. We selected the initial conservative parameters based on the chemistry between components and previous studies of amphiphilic molecules, and then adjusted them to obtain accurate self-assembly behavior of each component in the solvent (water).

**Table 1** DPD conservative force parameters for beads of CPCl and water (in units of  $k_B T/d_0$ ) †

	W	N	M	C
W	25	25	25	80
N	25	25	25	80
M	25	25	50	80
C	80	80	80	25

† "W" represents water bead. The pyridinium headgroup of CPCl is represented by two "M" and "N" beads while "C" beads make up the CPCl hydrophobic chain (Figure 5).

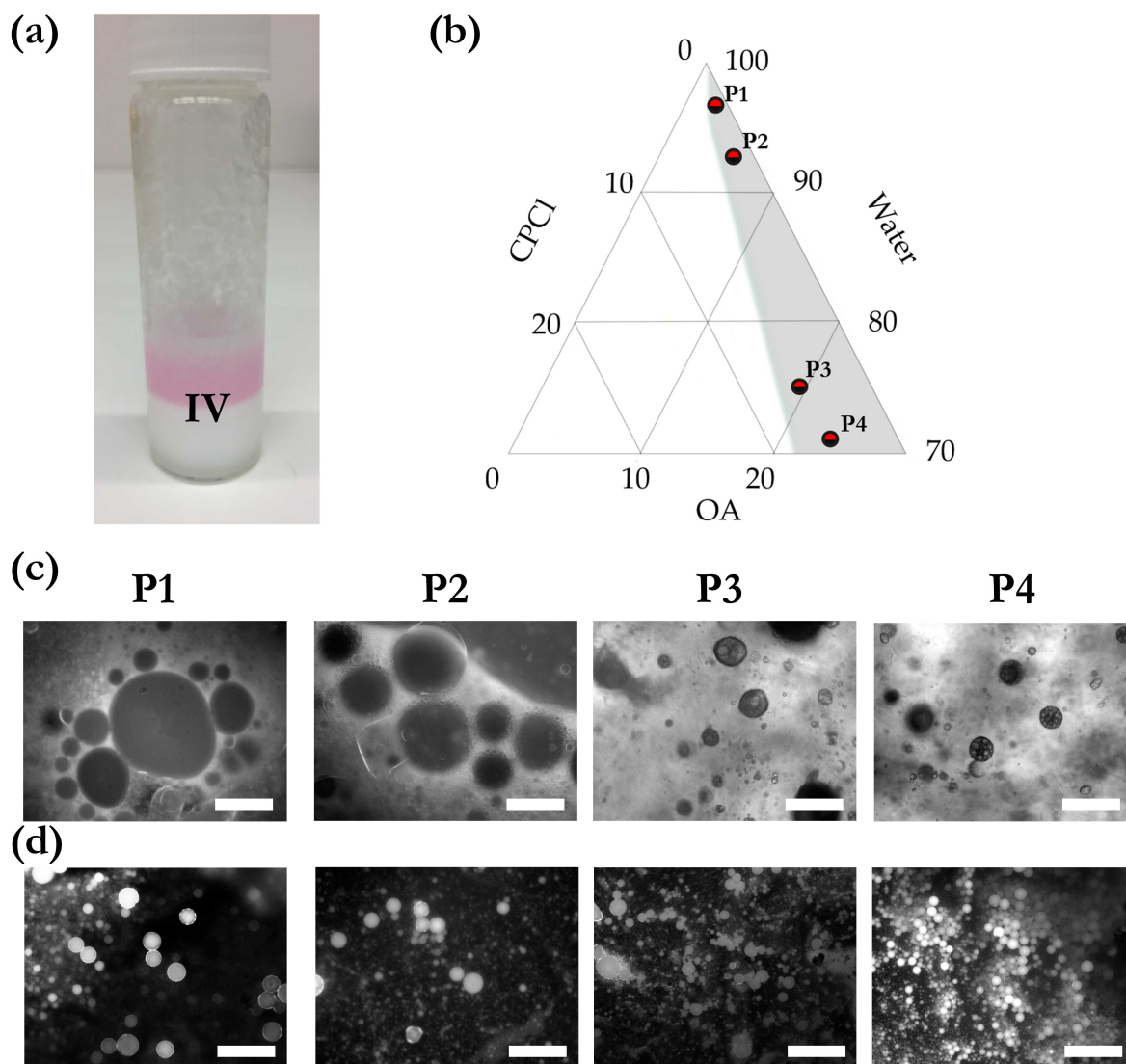


**Fig. 4** (a) Photograph of a typical sample in the region IV (phase separated) where oleic acid is stained with the red fluorescent dye (at the concentration of  $0.01 \text{ mg mL}^{-1}$ ). (b) A ternary phase diagram indicating sample location and composition. Fluorescence optical micrographs for (c) the top phases corresponding to water-in-oil emulsions and (d) the bottom phases consisting of oil-in-water emulsions (scale bars are  $200 \mu\text{m}$ ). The dark and light regions indicate water and oil domains, respectively.

#### CPCI parameterization based on its self-assembly behavior in water

Experiments predict that for a certain range of concentration, the amphiphiles aggregate into well-ordered structures in which the contact of their hydrocarbon tails with solvent (usually water) is minimized.<sup>2</sup> Formation of the same mesostructures has been observed in DPD studies because of the strong repulsion between the chain beads and the solvent beads, mimicking the hydrophobic effect for hydrocarbon chains in water.<sup>37</sup> A convenient parameter for analyzing the resulting structures of amphiphilic systems is the critical packing parameter  $CPP = v/a_0l_c$  (where  $a_0$ ,  $v$ , and  $l_c$  are the optimum headgroup area, chain volume, and chain length of the molecule, respectively).<sup>2</sup> CPCI which is a cationic surfactant, has a bulky charged headgroup (pyridinium) and one hydrocarbon tail and hence, for CPCI,

we can estimate that CPP lies roughly around  $\sim 1/3$  for the concentration range of our interest ( $50 - 560 \text{ mM}$ ). Specifically, the SAXS measurements results for pure CPCI solutions as shown in Figure 2a and reported in other studies<sup>2,29,60,61</sup> indicate that at lower concentrations CPCI molecules self-assemble into spherical micelles while for higher concentrations, the micelle becomes nonspherical (ellipsoidal), until they transform eventually into oblate ellipsoidal (disk-like). This self-assembly behavior of CPCI is most likely due to the fact that once the CPCI micelle becomes larger and the aggregation number increases, the crowding of hydrocarbon chains at the center of the micelle decreases the configurational entropy of the chains. This decrease in entropy results in formation of an ellipsoidal structure to accommodate more surfactant molecules in the micelles.<sup>2,60</sup> Due to the bulkiness of the pyridinium headgroup, the spherical micelles

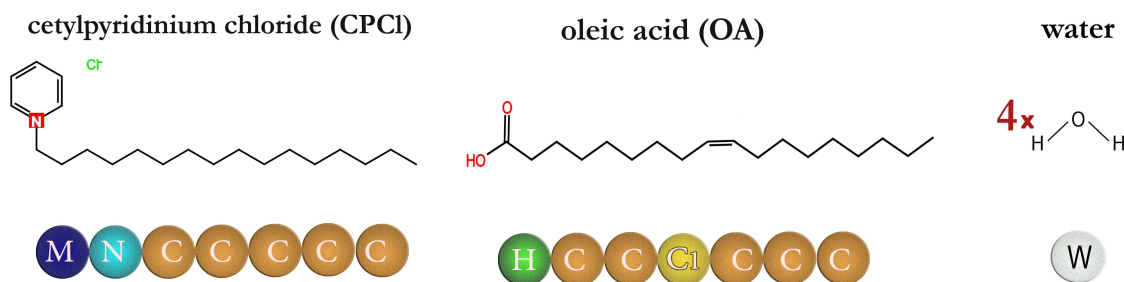


**Fig. 5** Coarse-grained mapping of CPCI and OA molecules used in DPD simulations. 3-4 hydrophobic alkyl groups were set as a single type "C" bead (orange). The pyridinium headgroup was represented by two beads; a "M" bead (navy blue) and a "N" bead (light blue), and the carboxyl headgroup of oleic acid was represented by a "H" bead (green). The "C1" bead type is distinguished from other "C" type beads in order to include a bending stiffness for representation of the OA double bond in the simulation. Each water bead ("W") represents four water molecules (See Experimental and method section) and is invisible for clarity in all simulation snapshots.

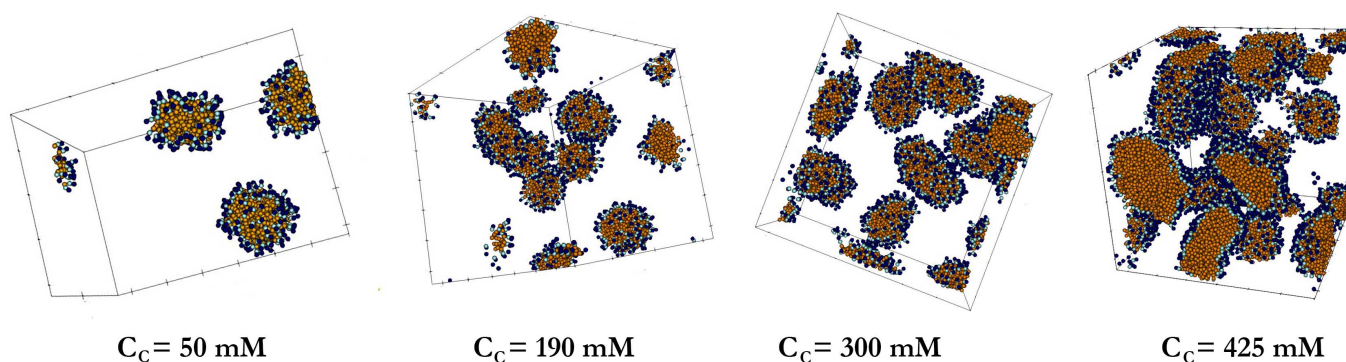


**Fig. 6** Snapshot of simulated equilibrium morphologies of CPCI surfactant aggregates in water (as solvent) at different CPCI concentrations ( $C_c$ ). The water beads (W) are hidden for convenient observation.

transition into disk-like micelles rather than cylindrical micelles since flatter surface accommodates greater numbers of micelles at high concentrations (425 mM).<sup>60</sup> At lower CPCI concentration (190 and 300 mM), however, a coexistence of spherical and disk-like micelles is observed in the DPD simulations since the surfactant concentration is not high enough to induce transitioning of all spherical micelles into disk-like micelles.

Based on these discussions, the conservative interaction parameters for CPCI beads ("M", "N", "C") are adjusted accordingly to achieve such self-assembly behavior. These interaction values are reported in Table 1. Although the DPD simulations do not have electrostatic charge, its short-ranged effect is represented by making headgroup beads more strongly repelled from each other through the conservative interaction parameters. Therefore, the interaction parameter between "M" beads is made highly repulsive ( $a_{MM} = 50$ ) as the pyridinium headgroup (a benzene ring with charged interaction) is bulky. Furthermore, with the mapping used here for CPCI, the volume occupied by the pyridinium headgroup is well enforced since each bead in simulation has a volume of  $120 \text{ \AA}^3$  which is almost equal to the volume of the pyridinium headgroup of CPCI ( $\approx 131 \text{ \AA}^3$ ).<sup>72</sup> The conservative interaction parameter between the water beads ( $a_{WW}$ ) is chosen equal to 25 to correctly describe the compressibility of water.<sup>57</sup> It is worth noting that all beads in DPD simulation are repulsive to each other and these values

determine the extent to which different types of beads are repulsive to one another. The phase behavior of CPCI in water obtained according to interaction parameters in Table 1 is shown in Figure 6. These snapshots demonstrate the structures that form in DPD simulation at different concentrations of CPCI solutions (50-425 mM), consistent with the experimental data of pure CPCI solutions.<sup>60,61</sup>

The diffusion coefficient of CPCI micelles ( $D_{mic}$ ) is used to map elapsed times in our mesoscale simulation of pure CPCI in water onto real times. The average diffusion coefficients of the CPCI micellar aggregates can be obtained from Stokes-Einstein relationship:

$$D_{mic} = \frac{k_B T}{6\pi\eta R_h}, \quad (7)$$

where  $k_B$  is the Boltzmann constant,  $\eta$  is the solvent viscosity,  $T$  is the absolute temperature, and  $R_h$  is the radius of the surfactant aggregates.<sup>60</sup> Hydrodynamic radius ( $R_h$ ) of CPCI micelle at a concentration range of 250-400 mM was reported to be 1-2 nm based on dynamic light scattering (DLS) measurements.<sup>60,61</sup> Given the water viscosity, the diffusion coefficient of CPCI micelles can be calculated to be  $D_{mic} \sim 120\text{-}250 \mu\text{m}^2 \text{ s}^{-1}$ . This value is in the same order of magnitude as the diffusion coefficient of other ionic surfactants such as hexadecyltrimethylammonium bromide (HTAB) with a diffusion coefficient of  $100 (\mu\text{m}^2 \text{ s}^{-1})$ <sup>73</sup> or sodium dodecyl sulfate (SDS) micelles with a diffusion coefficient of 100-

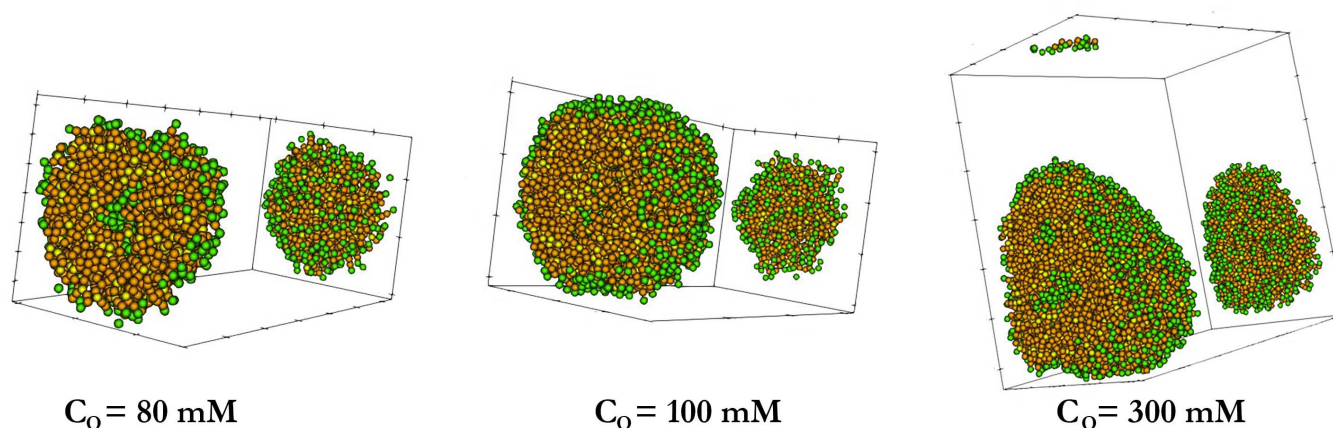


**Fig. 7** The snapshots of equilibrium morphologies of oleic acid (spherical aggregate) in water (as solvent) at different OA concentrations ( $C_o$ ).

$150 \mu\text{m}^2 \text{s}^{-1}$ .<sup>74</sup> In the simulations, the dimensionless diffusion constant of the CPCI micelles,  $D' = D_{mic}\tau/d_0^2$ , is obtained via the mean-square displacement of the constituent beads of the CPCI molecules. For instance, for the 425 mM CPCI solution in the simulation box  $(32d_0)^3$ , using  $D_{mic} \sim 120 \mu\text{m}^2 \text{s}^{-1}$  and the value  $D' = 0.0097$  from the simulations, we find the time scale  $\tau \sim 0.04 \text{ ns}$ . Accordingly, one simulation time step ( $\Delta t = 0.02\tau$ ) corresponds to  $\Delta t = 0.8 \text{ ps}$  of real time. Thus, the total time for the formation of micelles, which occurs near 200,000 time steps, is equivalent to  $0.16 \mu\text{s}$  in this case.

**Table 2** DPD conservative force parameters for beads of OA and water (in units of  $k_B T/d_0$ ) †

	W	H	C1	C
W	25	20	80	80
H	20	15	50	50
C1	80	50	25	25
C	80	50	25	25

† "W" and "H" beads represent water and OA headgroup, respectively while "C" and "C1" beads constitute the OA hydrophobic chain (Figure 5).

### OA parameterization based on its self-assembly behavior in water

Using molecular dynamics, Janke et al. studied the aggregation behavior of oleic acid in water as a function of protonation of headgroup (hence pH) and concentration.<sup>75</sup> Based on this study which is supported by experimental results,<sup>76,77</sup> and considering the pH range of our system measured previously,<sup>78</sup> we expect to have "oil phase" rather than micelles or vesicles. By "oil phase" here we mean spherical aggregates (like small droplets of oil) with OA headgroups arranged on the surface, but lacking a large aqueous interior and a bilayer structure. In order to have the described aggregation behavior for OA in water, the conservative interaction parameters as provided in Table 2 were used. The resulting morphologies for the OA in DPD simulation at different concentrations are shown in Figure 7, in agreement with the microscopic simulations<sup>75</sup> as well as experimental studies.<sup>76</sup> The structure obtained here is the same

"oil phase" with spherical morphology that we expected. There is no indication of vesicular structures since neither a large water interior cavity nor bilayer sheets are observed.<sup>75,77</sup> Within the observed spherical aggregates, the OA molecules arranged themselves with the headgroups positioned on the surface, which is expected to minimize the surface tension. The small amount of water within the macroscopic OA aggregates is expected in phase separated liquid mixtures.<sup>75,76,79</sup>

**Table 3** DPD conservative force parameters for all beads.  $\epsilon$  denotes the conservative force parameter for the interaction between headgroups of OA and CPCI (in units of  $k_B T/d_0$ ) †

	W	N	M	H	C	C1
W	25	25	25	20	80	80
N	25	25	25	$\epsilon$	80	80
M	25	25	50	$\epsilon$	80	80
H	20	$\epsilon$	$\epsilon$	15	50	50
C	80	80	80	50	25	25
C1	80	80	80	50	25	25

† Water beads are represented as "W". "M" along with "N" represents CPCI headgroup while OA headgroup is shown as "H". "C" and "C1" beads constitute the hydrophobic chain of both CPCI and OA (Figure 5).

### Dilution of CPCI solutions by varying OA content in DPD simulation

The validity of our model for the CPCI and OA was examined by the reproduced self-assembly behavior of each component in solvent (water). Now the phase behavior of the ternary mixtures of CPCI-OA-water is studied with an incremental increase of OA concentration in the aqueous CPCI solution. For doing so, all the interactions between beads are listed in Table 3, but the only force parameter to be determined is for the interaction between headgroups of OA and CPCI, i.e.,  $a_{MH}$  and  $a_{NH}$  (illustrated as  $\epsilon$  in Table 3). Hence, the simulations of the ternary system with all three components are performed in three scenarios with different headgroup interactions to investigate its effect on the resulting structure. This interaction between headgroups is quantified by the DPD conservative force parameters ( $\epsilon = a_{MH}, a_{NH}$ ) and is

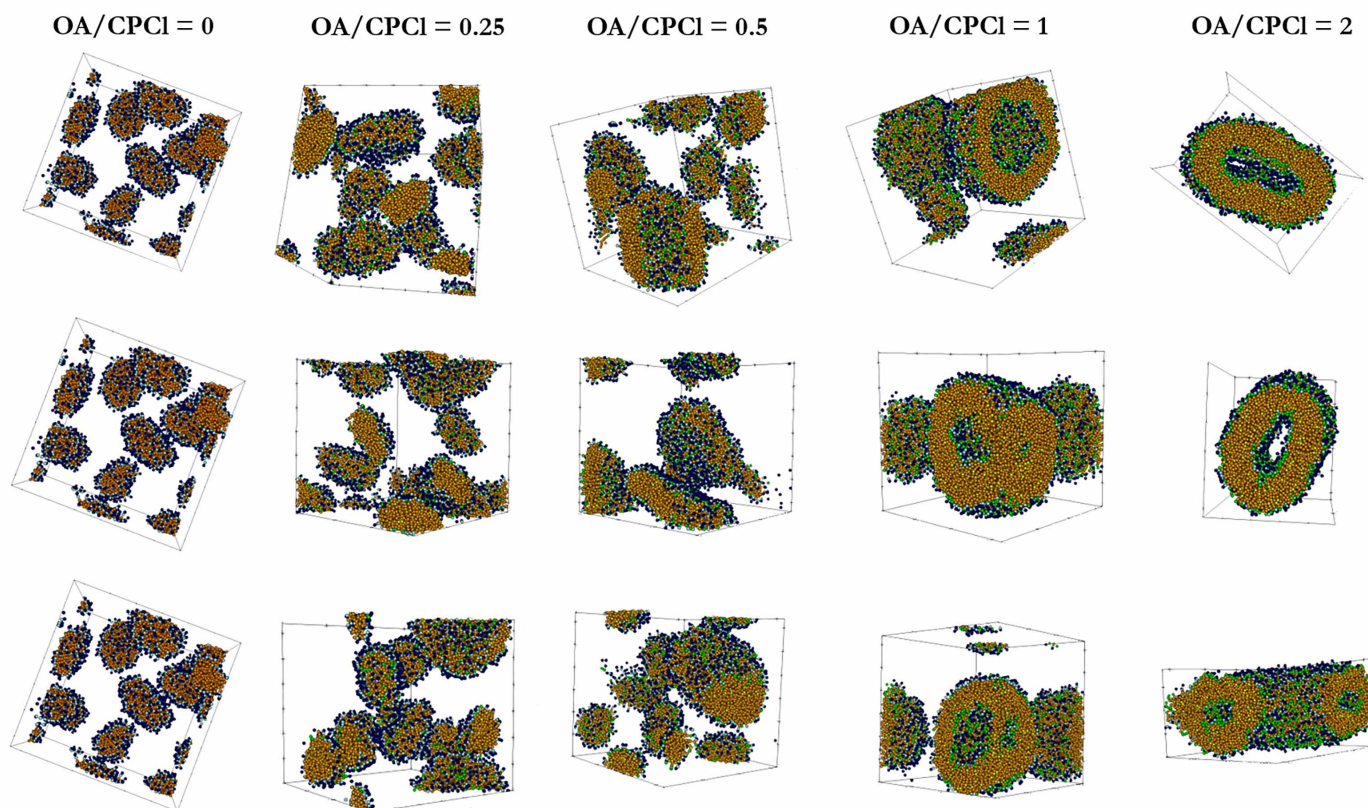


**Fig. 8** Effect of the conservative force parameter ( $\epsilon$ ) for interaction between headgroups of CPCI and OA on the morphologies obtained for the system upon increasing the concentration of OA. The CPCI concentration ( $C_c$ ) is 300 mM in all simulations. Top row ( $\epsilon = 15$ , attractive), middle row ( $\epsilon = 25$ , neutral), bottom row ( $\epsilon = 50$ , repulsive). For the OA/CPCI = 0 (first column), same DPD snapshot (of pure CPCI in water at  $C_c = 300$  mM) is illustrated for all three scenarios since no OA molecule and hence, no  $\epsilon$  is present in the simulation to make any difference.

varied from  $\epsilon = 15$ , to  $\epsilon = 25$ , and  $\epsilon = 50$  to represent a wide range of interactions between neutral carboxyl headgroup of OA and pyridinium headgroup of CPCI. The attraction between headgroups is created by setting  $\epsilon = 15$ , which being lower than  $a_{ww} = 25$ , causes the headgroups to prefer associating with each other instead of being solvated. A value of 50 for  $\epsilon$  makes the headgroups highly repulsive toward each other in a sense that they prefer solvation while the value of 25 ensures that the OA and CPCI headgroups have no preference between being solvated and being associated with each other. The phase behavior of the system at constant 300 mM CPCI concentration and varying OA/CPCI molar ratios for these three scenarios are provided in Figure 8.

In these snapshots and for all three scenarios, a morphological transition is seen which starts with elongated micelles of pure CPCI solution (OA/CPCI = 0, first column Figure 8) that gradually merge, becoming larger in size (for OA/CPCI = 0.25 and 0.5, second and third columns Figure 8) once the simulation is run with more OA molecules that are incorporated as a result of their hydrophobicity. With further increase in OA concentration, these enlarged micelles form patches which attach to each other and create vesicular structures (OA/CPCI = 1, fourth column in Figure 8). The vesicles become elongated upon further increase in the concentration of oleic acid, to the extent that it leads to

flatness of the vesicles, eventually transforming into quasi-planar bilayer sheets that are connected at the end (OA/CPCI = 2, fifth column in Figure 8). Scenarios with  $\epsilon = 15$  (attractive) and  $\epsilon = 25$  (neutral) showed almost exactly the same behavior whereas in scenario with  $\epsilon = 50$  (repulsive) as the interaction parameter, the structure is only affected at the highest OA/CPCI molar ratio (OA/CPCI = 2). Therefore, it can be concluded that varying the interaction between headgroups from attractive to repulsive does not greatly impact the microstructure for OA/CPCI molar ratios lower than 2. However, for obtaining the ternary phase diagram using DPD, a conservative force parameter ( $\epsilon$ ) of 25 is selected for the rest of this study as this value agrees with the chemistry of interaction between neutral carboxyl headgroup of OA and pyridinium headgroup of CPCI which is expected to be associated with cosurfactancy.<sup>29,80</sup> With the established interaction parameterization, a number of representative data points from the phase diagram of this ternary system were selected to compare the simulation results with experiments. Once the structure of each region in the ternary phase diagram is characterized using simulations, to ensure the results would not change if  $\epsilon$  was chosen as  $\epsilon = 15$ , one composition from each region is selected and by reducing  $\epsilon$  from 25 to 15, simulations are run again. The DPD results of these simulations show no apparent changes in terms of structure morphology (Figure S3,

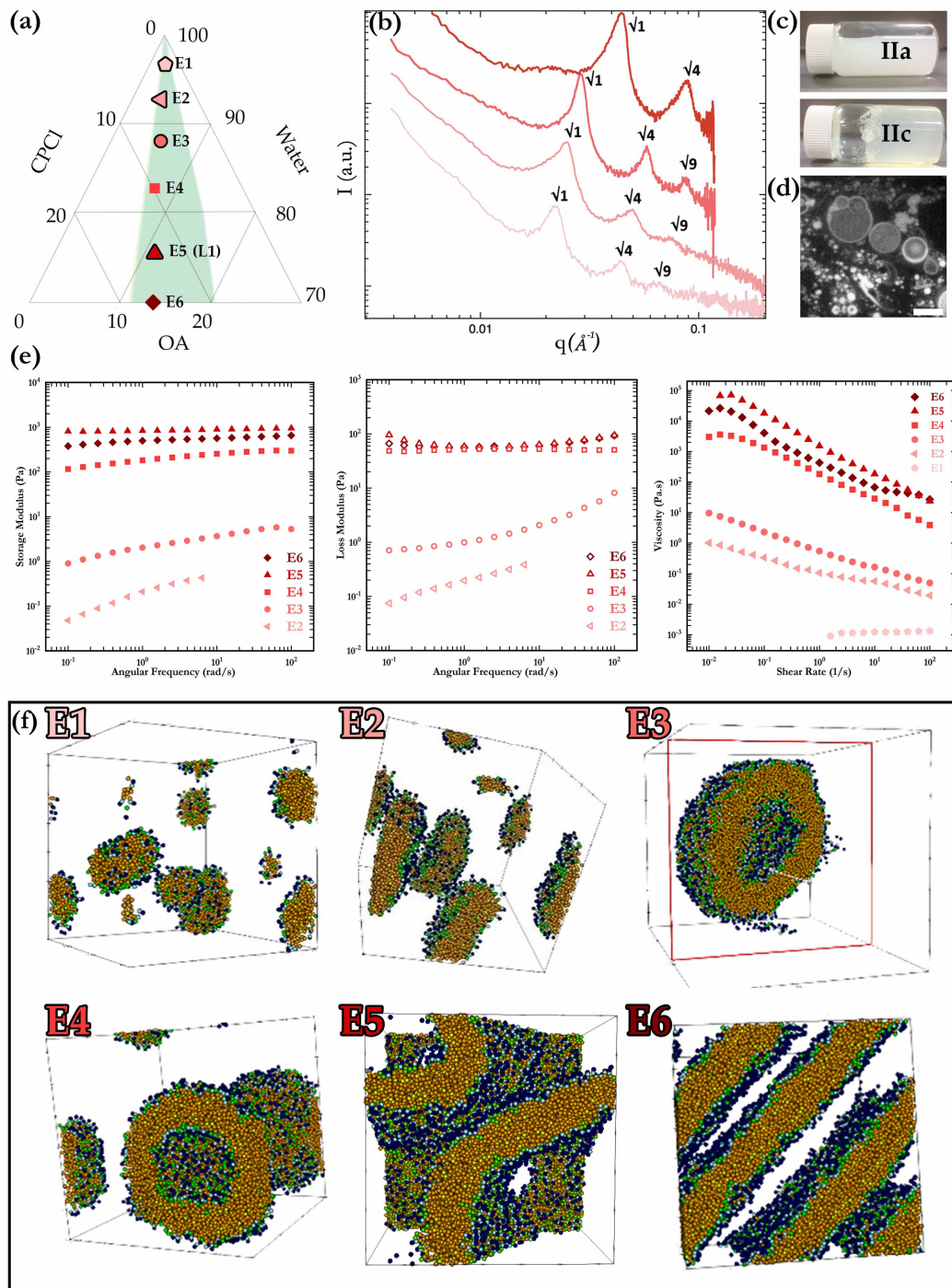


**Fig. 9** Vesicle-to-lamellar transition observed for the compositions with an equimolar mixing ratio of CPCI and OA with decreasing water content. The compositions in the ternary phase diagram are expressed in terms of weight percent. (a) Location of studied samples on the OA/CPCI equimolar line within the region II of the ternary phase diagram. (b) SAXS patterns corresponding to the data points shown on the diagram (a) demonstrating major peaks indicative of  $L_{\alpha}$  phase. (c) Different sample behavior observed for the system with a thin turbid phase "IIa" forming at the top and a thick semitransparent phase "IIc" at the bottom of the line. (d) Vesicular structures observed under confocal microscope for samples at top of the region II (scale bar represents  $13 \mu\text{m}$ ). (e) Plots of rheological measurements. From left to right: storage modulus and loss modulus curves versus angular frequency obtained from frequency sweep tests and shear viscosity as the function of shear rate. Data of dynamic frequency sweep for "E1" is not provided in the plots as they were affected hugely by instrument inertia. (f) DPD snapshots illustrating a transition from vesicular structure to lamellar structure with the decrease in water content along the OA/CPCI equimolar line.

ESI<sup>†</sup>).

### Vesicle-to-lamellar morphological transition along OA/CPCI equimolar line

First, we specifically investigate the samples with an equal molar ratio of CPCI and OA (labeled "E1-E6" in Figure 9a).

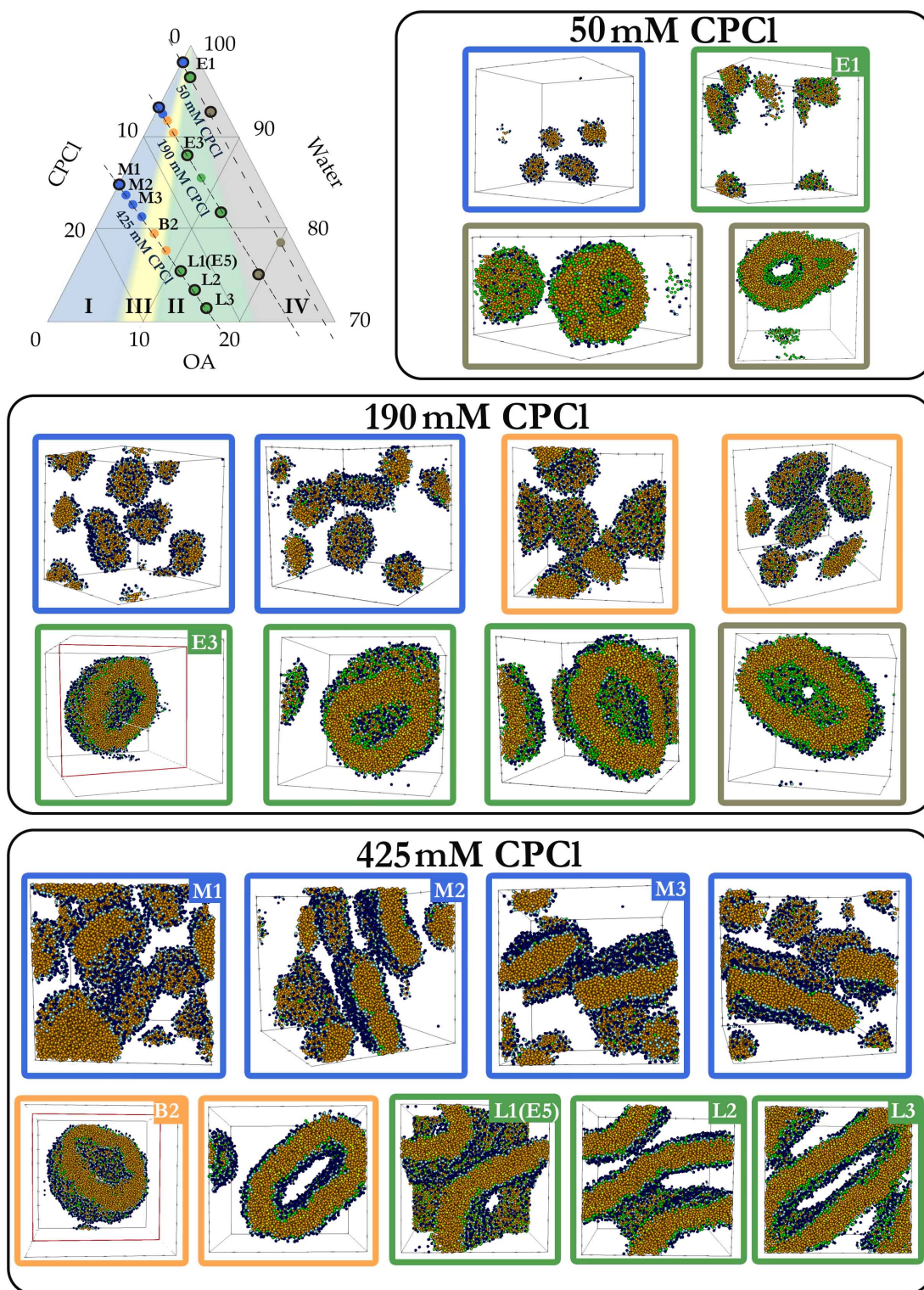


**Fig. 10** DPD simulations of different compositions along with their locations on constant CPCI concentration lines in the ternary phase diagram. The compositions in the ternary phase diagram are expressed in terms of weight percent. The snapshots show the final morphology of each data point in DPD simulations and the frame colors show the color corresponding to the region characterized for each composition experimentally.

SAXS measurements for these samples indicate the formation of vesicle or lamellar structures (Figure 9b) where there is a shift in the peaks towards higher  $q$  with a decrease in the water content. This shift indicates that the repeat spacing

of these layers (interlayer spacing,  $D = 2\pi/q^*$ ) is decreasing from  $D \approx 29$  nm to  $D \approx 14$  nm with the decrease in the water content (*i.e.*, an increase in the surfactant concentration from 50 mM to 425 mM). This observation means that as we

move down on the OA/CPCl equimolar line, the solution state changes from water-like (vial "IIa" in Figure 9c) to a thicker gel (as the water layer between bilayer sheets shrinks), and finally exhibits gel-like characteristics (vial "IIc" in Figure 9c), possibly due to a transition from dilute-vesicles to close-packed vesicles and lamellar. An explanation for the vesicle-to-lamellar transition is that an increase in OA concentration can lead to less efficient repulsion between the polar groups of CPCl surfactants in the vesicles, favoring lower-curvature sheet-like structures as opposed to the multilamellar curved vesicles.<sup>35,80,81</sup> Confocal microscopy confirms the presence of vesicular structures for sample "E1" (Figure 9d) with the highest water content along this line.

For these samples on the OA/CPCl equimolar line, the rheological tests including amplitude sweep, frequency sweep, and steady shear flow were carried out. The amplitude sweep curves are provided in Figure S1c (ESI<sup>†</sup>). For sample "E1", measurement of the shear moduli in oscillatory tests was not possible due to dominant instrument inertia, similar to samples in the micellar region (I). While compositions "E2" and "E3" exhibit limited frequency dependency for  $G'$  and  $G''$ , shear moduli of compositions "E4-E6" showed to be independent of frequency (Figure 9e). The lack of frequency dependency of shear moduli for compositions "E4-E6" indicates a more structured sample compared to "E1-E3" which is also evidenced by their flow behavior (Figure 9c). Furthermore, both storage ( $G'$ ) and loss ( $G''$ ) moduli generally increase with a decrease in water content along the OA/CPCl equimolar line. Based on the flow sweep results (right-hand side of Figure 9e), all samples exhibit the shear-thinning behavior except for the sample "E1" which shows a constant viscosity as expected. The value for the viscosity of most samples at any shear rate decreases by decreasing the water content with the exception of the sample with the lowest water content ("E6"). This sample ("E6") exhibits a drop in viscosity-shear rate curve in agreement with frequency sweep results where a slight to moderate drop occurred for both shear moduli compared to the sample "E5" and the reason for this behavior remains as yet unknown. Furthermore, for this sample ("E6") a shoulder at medium shear rates is observed, similar to the flow behavior of other samples with the lowest water content (e.g., "L2" and "L3" in Figure 3b). In conclusion, a significant change in the rheological behavior is observed along the OA/CPCl equimolar line based on these rheological results, which could corroborate the vesicle-to-lamellar morphological transition hypothesis mentioned earlier.

We also investigated the vesicle-to-lamellar morphological transition using DPD simulation of the same data points located on the OA/CPCl equimolar line. The snapshots of these simulations are shown in Figure 9f. Except for the top two compositions along the equimolar line with the highest water contents ("E1" and "E2" in Figure 9a) that show neither vesicles nor lamellar (rather micellar) structures in DPD simulations, for the rest of the data points, we observe a transition from vesicle to lamellar structure as the water content decreases, supporting the vesicle-to-lamellar transition. Simulation results

in the larger box with  $L = 64d_0$  (that will be discussed later in the system size dependence section) indicates the same vesicle-to-lamellar transition, but an upward shift is observed for the morphological transition trend (micelle-to-vesicle-to-lamellar) along the equimolar line; i.e., the composition "E2" shows the formation of vesicles and composition "E4" is in fact a lamellar morphology which is forced to form a vesicle structure in the smaller simulation box.

### Micelle-to-lamellar morphological transition along constant CPCl concentration lines

To investigate whether the same micelle-to-lamellar morphological transition observed in experimental results (from the region I to II in Figure 1, explained in Experimental results section) occurs in the simulation, several compositions along three lines with constant CPCl concentrations (50, 190, and 425 mM) in the ternary diagram were simulated and results are provided in Figure 10. The morphological observations in simulations and experiments for these compositions are in good agreement. In accordance with experimental results, the snapshots of DPD simulations in the region I ( $L_1$  phase) show a micellar structure with both spherical and disk-like elongated micelles (snapshots with a blue frame in Figure 10 and Movie S1, ESI<sup>†</sup>). For all of the compositions in the region II ( $L_\alpha$  phase) except for the one with 50 mM CPCl concentration (which will be explored in the system size dependence section), structures obtained in DPD follow the morphological observation of experiments with the formation of bilayers (either lamellar or vesicle structures as shown in DPD snapshots with a green frame in Figure 10 and Movies S2-S4, ESI<sup>†</sup>). We can go further and approximate the real time needed for the formation of lamellar structures by matching the self-diffusion of OA molecules within a bilayer between the DPD simulation and reported values. The dimensionless self-diffusion coefficient of OA molecules (expressed as  $D'$ ) within a bilayer structure is obtained in DPD simulation by displacement of the "H" bead of OA and scales with  $D\tau/d_0^2$ , where  $D$  has the reported value of  $35 \mu\text{m}^2 \text{s}^{-1}$ .<sup>82</sup> For the composition with 425 mM CPCl and the highest content of OA (labeled "L3" in Figure 3b diagram), a  $D' \sim 0.0095$  is obtained as the output value which yields  $\tau = 0.138 \text{ ns}$  and a time step of  $\sim 2.7 \text{ ps}$ . Then a run of 1.5-1.8 million steps which is needed to form a lamellar structure represents around  $4.5 \mu\text{s}$  of real time for this composition.

In the biphasic region (III), DPD snapshots for 190 mM CPCl compositions show disk-like micelles while for compositions with 425 mM CPCl concentration, curved bilayers like vesicles are observed (snapshots with an orange frame in Figure 10 and Movie S5, ESI<sup>†</sup>). Given the system size that the simulation technique is capable to capture and considering the length scale in which the bilayers separate out of the micellar bulk solutions (typical of a  $L_1/L_\alpha$  biphasic region), we do not expect to see the coexistence of micellar and lamellar structures in simulations. However, the morphologies that were reported to be  $L_1/L_\alpha$  biphasic in experiments can be interpreted in the simulation to be the intermediate morphologies between micellar and lamellar structures. For example, in the simulations for constant 425

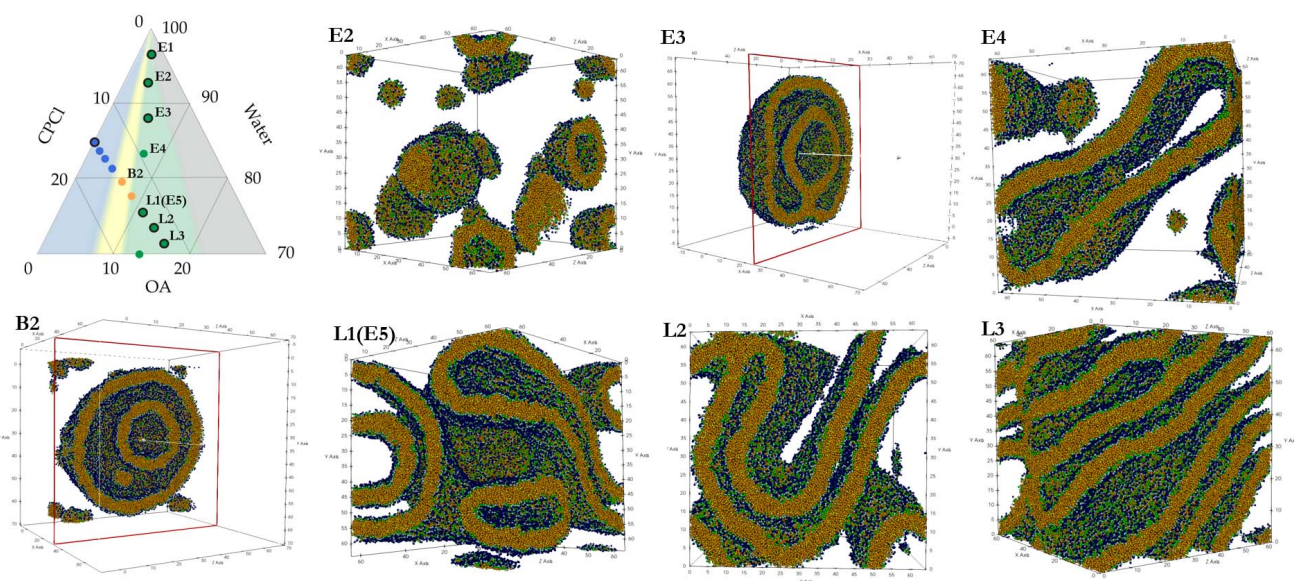


**Fig. 11** Location and DPD snapshots of compositions simulated in the larger simulation box  $(64d_0)^3$ . These snapshots should be compared with the corresponding snapshots in Figures 9 and 10 which are simulated in a box size of  $(32d_0)^3$ . The color of each data point in the ternary diagram corresponds to the region characterized for each composition experimentally. The compositions in the ternary phase diagram are expressed in terms of weight percent. For composition "E2", the formation of unilamellar vesicles is shown which is not captured in the simulation box  $32d_0^3$  (Figure 9f). When composition "E3" is run in the simulation box  $(64d_0)^3$ , a multilamellar vesicle is formed. The vesicle structure is cut in half to better show two bilayer sheets and the inner part of the vesicle. Composition "E4" with 300 mM CPCI on the equimolar line exhibits two large bilayer patches with a fluctuating curvature and connected junctions at two ends of the simulation box. A multilamellar vesicle observed for composition "B2" that the small box did not capture because each axis of the box was smaller than the domain spacing of the vesicle. The vesicle structure is cut halfway through the box axis for easier illustration of two bilayers. For composition "L1" (also labeled "E5" in Figure 9a) with a CPCI concentration of 425 mM, a single folded unilamellar which spans across the simulation box axis is observed along with a unilamellar vesicle at the center bottom. For composition "L2", an extreme curvature is observed for bilayers which was not captured by the small box size ( $L = 32d_0$ )<sup>3</sup> in Figure 10. The formation of flat lamellar structure is confirmed for composition "L3" in the larger box too, but with some connecting junctions along the bilayers.

mM CPCI concentration line (snapshots with an orange frame in the last row, Figure 10), the two points in the biphasic region (III) appear to be significantly different from the micellar (I) and lamellar (II) regions with extremely curved structures like a vesicle or bilayer patches that are connected at both ends.

For the compositions located in the phase separated region (IV), the morphologies that are observed in the DPD simulations are either two bilayer patches connected at their ends or a vesicle (snapshots with grey frame in Figure 10) which agrees with structural features identified for the top phase in SAXS results (Figure 2d). However, similar to the discussion mentioned earlier regarding the system size that the simulation technique can capture and considering the fact that the phase separation in our system occurs at much larger macroscopic scales, it is not possible to observe the macroscopic phase separation in DPD.

### System size dependency and domain spacing of structures in DPD simulation

A system size dependency analysis is carried out (see Experimental and method section) to investigate the effect of the simulation box size on structures and whether the small size of the simulation box is the reason for some discrepancies observed in morphologies between simulation and experiments (mostly in the region II). The location of samples in the ternary phase diagram and their corresponding DPD snapshots in the larger

simulation box (with the linear size of  $64d_0$ ) are provided in Figure 11 and will be discussed in the following.

As for one of the two compositions on top of the OA/CPCI equimolar line ("E2"), the larger box simulation demonstrates the formation of multiple unilamellar vesicles, in agreement with SAXS results while for the other one ("E1") which has the highest water content, in contrast to SAXS results, no vesicular or lamellar structure is observed even in the larger simulation (Figure S4, ESI<sup>†</sup>). Instead, a micellar morphology is observed that interestingly, agrees with the rheological behavior for this composition (right plot in Figure 9e), where the dominant instrument inertia in oscillatory tests and constant viscosity along the measured shear rate range suggest a micellar phase for this composition (similar to samples in the region I). Although it is true that for capturing accurate representation of the morphology for this composition, even a much larger box than  $(64d_0)^3$  is needed, performing such simulations falls out of the objective of this work since it would be prohibitively expensive in computer time.

In the region II ( $L_\alpha$  phase), although we were not able to assign the  $L_\alpha$  phase to vesicular or lamellar structure solely based on SAXS measurements (as discussed in II. Lamellar/vesicle region ( $L_\alpha$ ) section of experimental results), if any sample within this region or even in the biphasic region (III) were to be assigned a vesicular morphology, SAXS measurements suggest vesicles to

be multilamellar because of multiple peaks in SAXS pattern, but the structures observed in the small box simulations (DPD snapshots in green frames in Figures 9 and 10) are unilamellar vesicles. We hypothesize that multilamellar vesicles are not observed in these DPD simulations because of the small box size ( $L \approx 32 \times d_0 \approx 22$  nm, with  $d_0$  of 0.711 nm), since alternating self-assembled CPCL/OA bilayer sheets and water layers with a domain spacing of 10-40 nm could form multilamellar vesicles up to several hundreds of nanometers in size.<sup>33</sup> Interestingly, simulation results for compositions "E3" and "B2" in the larger box captures multilamellar vesicles (Figure 11) which supports the earlier hypothesis we made for not capturing such multilamellar vesicles because of small size of the simulation box. This observation suggests that the equilibrium structures are correctly represented when the simulation box is sufficiently large, and emphasizes the importance of performing system size-dependent simulations.

For composition "E4" on the OA/CPCL equimolar line with 300 mM CPCL concentration, a morphology comprising large bilayer patches with high curvatures is observed ("E4" in Figure 11). These bilayer patches are connected to themselves at both ends of box periodic boundaries. The curvature tends to move along these bilayers as the simulation evolves, indicating the fluid state of the aggregate, a true representative of liquid crystalline structure.<sup>1</sup> In contrast to what was observed here, this composition proved to yield a unilamellar vesicle in  $(32d_0)^3$  simulation ("E4" in Figure 9), proving the hypothesis we made earlier that such a vesicle is probably forced to form by periodic boundary conditions imposed by small simulation box.

As for composition "L1" (also labeled "E5" in Figure 11) which marks the beginning of region II along the constant 425 mM CPCL concentration line, a single folded unilamellar vesicle is observed which spans across the simulation box axis along with another unilamellar vesicle at the center bottom. Such structure is comparable with the one seen in the smaller simulation box in that both demonstrate the formation of bilayer sheets alternating between layers of water (Movie S2, ESI†). In particular, the simulation results in the larger box show that the two bilayer sheets leaving the box at the bottom right join the fragment of vesicle on the left which connects back to the large vesicle at the top right. Comparing such structure with structures in smaller box size simulations suggests that due to smaller simulation box size in Figure 9f and Figure 10, all the details of such structure including the extreme curvatures along bilayer sheets is not captured, unlike the larger simulation box in which the folding of bilayer sheets are completely depicted ("L1 (E5)", Figure 11).

For the composition labeled "L2", while the small simulation size  $(32d_0)^3$  shows an almost flattened bilayer structure (Figure 10) and captures just a slight curvature along these bilayer patches, the large simulation box (Figure 11) reveals the bilayers with a pronounced curvature. Such high curvatures reflect on the transition from curved vesicles to a flat lamellar structure. For the composition "L3" which has the highest OA content along the constant 425mM CPCL concentration line, the formation of a flat lamellar structure is confirmed in the large simulation box  $(64d_0)^3$  with a slight difference in the presence

of connecting junctions ("L3" in Figure 11), compared to the small box simulation ("L3" in Figure 10). The structure obtained for compositions "L2" and "L3" are both identified as lamellar morphologies composed of alternating self-assembled CPCL/OA bilayer sheets and water layers. The difference in curvature between the two samples is attributable to their difference in OA content, which can act to stiffen the bilayer and decrease curvature. The "L3" bilayer with its higher OA content, therefore, forms a flat lamellar microstructure (see Movie S4, ESI†) whereas the "L2" with decreased OA content exhibits a bilayer with extreme curvature (Movie S3, ESI†). The DPD snapshots of structure for other compositions which are simulated in the box size  $64d_0^3$  are not shown as there was no difference in the equilibrium morphology as a result of the change in the box size.

Although the domain spacings for lamellar structures in DPD simulation have been investigated mainly for diblock copolymers,<sup>83</sup> such study has not been reported for short-chain amphiphilic molecules like lipids or surfactant systems. Comparison of bilayer domain spacings for lamellar/vesicles in our system (region II) between simulation and experiments is difficult for two reasons. The first reason originates in the coarse-grained nature of the molecular species in DPD simulations. Each bead represents a small number of the corresponding atomic species, which results in a DPD water bead representing four water molecules. Such mapping does not affect the structural properties of the lamellar in equilibrium, *e.g.*, the bilayer thickness and area per molecule, but it can influence the trajectory followed by a simulation of multiple lamellar. Whereas water is a small molecule compared to surfactants and oleic acid in experiments and can readily pass through a CPCL/OA bilayer, a water bead in the simulations is comparable in size to the headgroups of the other species, and has a strong repulsion from the hydrophobic interior of the bilayer. For a system that is expected to form multiple lamellar in equilibrium which is the case here, the water gap spacing may depend on how the bilayers form and "seal" into their final box-spanning state. This is so because water beads require an extremely long time to diffuse from one water gap through a bilayer to the next water gap if the bilayers span the whole simulation box. We note that the CPCL/OA bilayers observed for lamellar/vesicle structures in simulation, as shown in Figure 11 for "L1-L3", are comparable with experiments as they yield a thickness of  $\approx 4$  nm (about twice the hydrocarbon chain length of CPCL or OA). The second source of discrepancy for the smaller water layer thickness at some parts than from those observed in experiments (see Experimental results section, Lamellar/vesicle region) could be due to the lack of long-ranged electrostatic repulsion between CPCL/OA layers in DPD simulations and large fluctuations originating in the small system size.

### Effect of OA polarity on inducing formation of bilayer structures

Although there are some minor differences in structures obtained from experiments and simulation, for both studies, it was observed that upon increasing the OA content, a phase transition from  $L_1$  (micellar solution) to  $L_\alpha$  (lamellar or vesicle) occurs. We

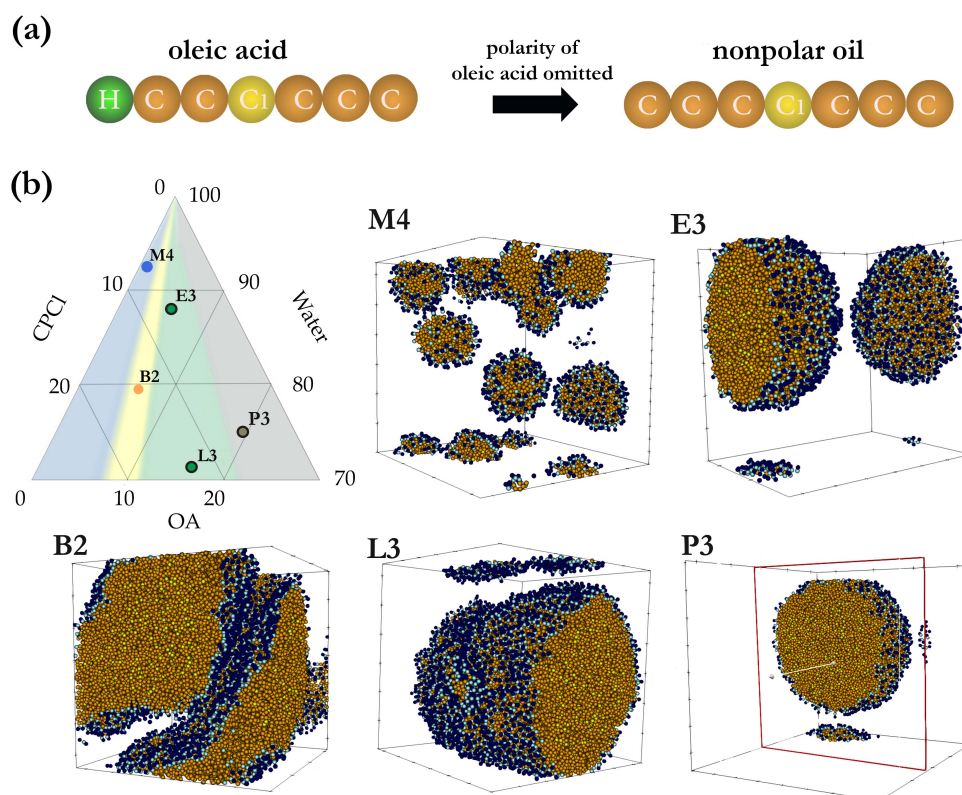


**Fig. 12** Effect of the polarity of OA headgroup on microstructure formation. (a) The polarity of oleic acid in these simulations is omitted by replacing the "H" bead type with a "C" bead type in the structure of the OA molecule. (b) Location and DPD snapshots of compositions simulated when polarity of the OA is removed.

hypothesize that such a morphological transition from micelles to lamellar/vesicle structure is due to cosurfactancy of oleic acid, similar to what was reported previously.<sup>29</sup> Owing to its polar headgroup, OA molecules behave as cosurfactants and hence, their packing in CPl aggregates is different from conventional oils with nonpolar headgroups.<sup>78</sup> That is, the aggregate volume is roughly doubled due to the dilution of the CPl headgroup and the formation of pseudo-double-chained surfactants (from the two single chains of surfactant and OA). Thus  $CPP(= v/a_0l_c)$  value increases from  $\sim 1/3$  (micellar) to  $>2/3-1$  (vesicles or lamellar).<sup>62</sup> This increase in  $CPP$  first leads to a transition of nearly spherical micelles to disk-like micelles (for lower CPl concentrations) rather than cylindrical micelles due to equal lengths of the alkyl chains of CPl and OA<sup>87</sup> or further growth of disk-like micelles (for higher CPl concentrations), and eventually induces aggregate transitions from disk-like micelles to closed (or vesicular) or flat bilayers. Previous studies have reported on the ionization of oleic acid (hence electrostatic interactions) to be the reason for such phase transition,<sup>33,80</sup> but this is unlikely to be the case here since the same phase transition was observed once OA was substituted by oleyl alcohol or oleylamine, both of which are neutral and will not be ionized in water.<sup>29</sup> This hypothesis is also supported by simulation results since the electrostatic interaction which is long-ranged is not represented in our DPD simulations, but the same phase behavior was observed which

indeed makes OA cosurfactancy the most probable reason for this micelle-to-lamellar transition. The main difference between our system and pure cationic systems<sup>35,80,88</sup> obtained from anionic and cationic surfactants where electrostatic interactions drive the morphological transitions is that the neutral form of the OA fatty acid and ionized CPl molecules are associated by hydrogen bonding instead of electrostatic interactions. The role of OA headgroup polarity on the formation of microstructures and morphological transitions in this system was explored by conducting additional simulations. Specifically, the "H" bead (green) of oleic acid (which represents the polar carboxyl group) is replaced with a "C" type bead (orange, Figure 12a) which had formed the hydrophobic chains in the prior simulations. With this mapping, the resulting oil molecule is only comprised of hydrophobic beads and the molecular structure of CPl remains unchanged (Figure 12a) so that the simulated system represents the phase behavior of a conventional surfactant-nonpolar oil-water system. The snapshots of DPD simulation for several compositions across the ternary diagram along with their locations are provided in Figure 12b. For the "M4" composition, no apparent qualitative change is observed, which is expected since a micellar structure is frequently observed for nonpolar oil systems.<sup>1,3</sup> Interestingly, for the rest of compositions (e.g., "B2", "L3", "P3", and "E3"), large oil domains are formed rather than the specific microstructures (e.g., vesicle/lamellar) that are identified when the oil component possesses polarity (OA).

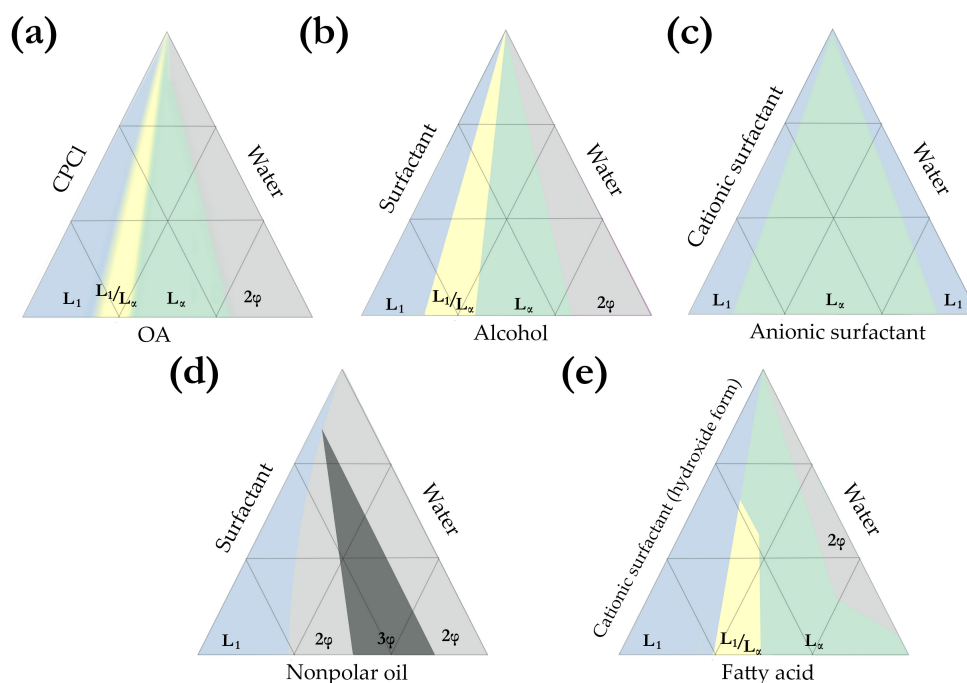


**Fig. 13** Comparison of the established ternary phase diagram with relevant surfactant systems. (a) Phase diagram of the ternary system of CPCI-OA-water established in this work. Typical phase diagram of various systems; (b) surfactant-alcohol-water,<sup>84,85</sup> (c) catanionic surfactant,<sup>86</sup> and (d) surfactant-nonpolar oil-water systems.<sup>1,3,67</sup> (e) Phase diagram of a specific fatty acid catanionic system.<sup>20</sup>  $L_1$ , denotes a micellar solution,  $L_\alpha$  a lamellar structure, and  $L_1/L_\alpha$  a two-phase region (with  $L_\alpha$  phase at the top and  $L_1$  at the bottom). Phase separated regions including two-phasic and three-phasic are shown as  $2\phi$  and  $3\phi$ , respectively. The overall topology of the phase diagrams is shown here with general features of each system, and hence, the lines and regions are not accurate.

Within these oil domains, neither aqueous interior nor bilayer structure is observed and CPCI surfactants arrange themselves at the interface with headgroup exposed to the surrounding water. These simulations are in agreement with experimental studies in that for ternary diagram involving a nonpolar oil, no lamellar/vesicle mesophase is observed.<sup>1,3,67</sup>

### Comparison of the established phase diagram with other surfactant ternary systems

As mentioned in the Introduction section, no reported ternary phase diagram for surfactant-liquid fatty acid-water is available to the best of our knowledge. Here, we discuss how our phase diagram relates to the available surfactant ternary systems including surfactant-alcohol-water (Figure 13b),<sup>84,85</sup> catanionic surfactant-anionic surfactant-water (catanionic, Figure 13c),<sup>86</sup> surfactant-oil-water (generic microemulsion systems containing nonpolar oils, Figure 13d),<sup>1,3</sup> and basic catanionic surfactant-fatty acid-water (also referred to as fatty acid catanionic, Figure 13e).<sup>20</sup> By comparing the ternary phase diagram reported here with the general features of these systems, it is revealed that the formation of micellar phase ( $L_1$ ) at left side of ternary diagram is typical for all systems.<sup>1,3,20,84–86</sup> Macroscopic phase separation which occurred at highest oil concentrations in our diagram is also observed in almost all other systems except for catanionic surfactant-anionic surfactant-water (catanionic) system.<sup>1,3,20,84–86</sup> In catanionic systems, two different micellar phases form at two sides of the ternary diagram as they contain

two types of surfactants and only one solvent (water) and the formation of a macroscopic phase separation is not expected.<sup>86</sup>

Phase sequence of our system ( $L_1$ - $L_1/L_\alpha$ - $L_\alpha$ - $2\phi$ ) shows the most resemblance to that of a generic surfactant-alcohol-water system (Figure 13b).<sup>84,85</sup> We hypothesize that this resemblance is due to the fact that alcohols (similar to OA in our system) act as a cosurfactant. In those systems, the alcohol chain size is a critical factor in alcohol cosurfactancy effect; longer alcohol chains make larger micelles and extend the liquid crystalline region, particularly that of the lamellar phase, far toward the water-rich corner, while this region is non-existent in the short-chain cosurfactants.<sup>84</sup> Similarly, in generic surfactant-oil-water systems (microemulsions), the cosurfactancy effect is not present as the oil is inert and nonpolar, and as a result, the formation of the lamellar region is not expected as depicted in Figure 13d.<sup>1,3</sup> In these systems, the phase separated region could exist as two- or three-phasic (with oil-in-water and water-in-oil emulsions and/or microemulsion phases), depending on the nature of surfactants and experimental conditions.<sup>67</sup>

Figure 13e depicts a specific case of catanionic system in which an oil-based fatty acid is used as the anionic surfactant and often referred to as fatty acid catanionic system.<sup>20</sup> This category of studied system is concerned with the catanionic surfactants in their hydroxide form (basic surfactant) with an attempt to make salt-free solutions.<sup>20</sup> Despite such difference and the fact that the used fatty acids in those systems are in their solid form at room temperature, we still observe features in the phase diagrams

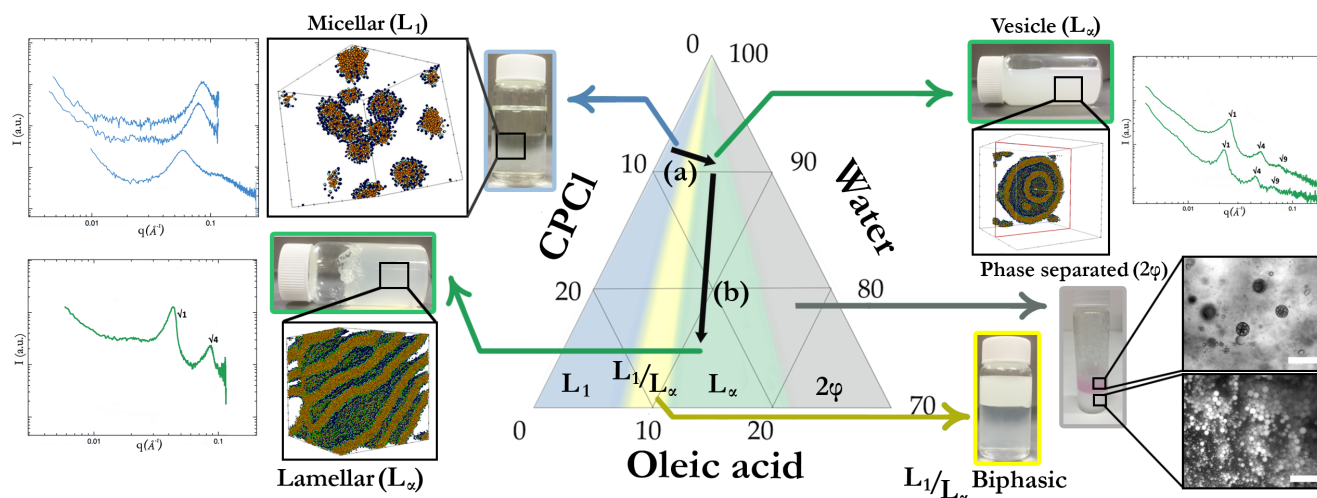


**Fig. 14** The ternary phase diagram of the CPCI-OA-water system and the morphological transitions (shown with arrows "a" and "b") characterized by both simulation and experimental techniques (scale bar represents 200  $\mu\text{m}$ ).

similar to our system (Figure 13e).

In all, the ternary phase diagram established here is a model system for surfactant-liquid polar oil-water system, which is an unexplored area. The fundamental knowledge regarding the ternary system shown here is also translatable to different associative surfactant systems.

### General remarks and consideration

Using experiments and simulations, we have mapped out a ternary phase diagram for an associative system of surfactant-polar oil-water and identified the morphological transitions across the diagram. The fundamental self-assembly principles revealed in this study are extendable to different associative surfactant systems involving cosurfactants and polymers. Combining experiments and simulations affords access to previously-inaccessible characteristic length scales of the system, *i.e.*, simulations relate molecular-scale dynamics to the experimental macroscale structures, and provides a better understanding of the underlying self-assembly processes, paving the way towards rational design of these assemblies for creating functional materials that operate at the mesoscale.

Specifically, in this study, experimental techniques (*i.e.*, SAXS, rheology, and optical microscopy) characterized the structural and viscoelastic properties of the self-assembled materials. DPD in this work served as an efficient mesoscale coarse-grained methodology for modeling the presented ternary system and successfully predicted morphological transitions across the diagram in accordance with experimental results. The relationship between characterized structure and properties enabled the verification of the phase behavior. Additionally, DPD results provided insight into the underlying self-assembly process and resulting self-assembled structures. Both experimental techniques and computational tools used here have their own individual limitations (*e.g.*, experimental setups can be limiting in terms of time and length scale while computer simulations need experimental validation), but the combination of the two techniques enables deeper fundamental insight into the

phase behavior of multi-component systems. Specifically, as captured by SAXS measurements and reproduced in DPD simulations, a micelle-to-lamellar transition (shown with arrow "a", Figure 14) is observed with an increase in the OA content of the surfactant solution (with constant surfactant concentration), in accordance with the significant change in the rheological behavior from Newtonian behavior (constant, rather low viscosity) to solid-like viscoelastic behavior with shear-thinning properties. Furthermore, along the OA/CPCI equimolar line, SAXS patterns indicate lamellar/vesicle structures, and rheological measurements and DPD simulations identify the vesicle-to-lamellar transition (shown with arrow "b", Figure 14) with decreasing water content. A phase separated region is also characterized as two emulsion phases (through optical microscopy), and its nanostructures are found to be lamellar/vesicle in both SAXS measurements and DPD simulations. Figure 14 presents these morphological transitions within the four distinct regions of the phase diagram which are characterized with the effective combination of experiments and simulations

### Conclusion

In summary, the phase diagram of a system of CPCI-OA-water is studied both experimentally and in simulation with a particular emphasis on microstructures and rheological properties. For the experimental part, based on the visual inspection and SAXS measurements, the water-rich corner of the phase diagram of our ternary system is explored and four distinct regions ( $L_1$ ,  $L_\alpha$ ,  $L_1/L_\alpha$  biphasic, and phase separated) are identified. The rheological properties corresponding to each region are shown to change significantly. While the  $L_1$  phase (micellar) shows low viscosity and  $L_\alpha$  phase (vesicle or lamellar) reveals typical solid-like viscoelastic behavior with shear-thinning properties, the  $L_1/L_\alpha$  biphasic region acts as a transitional region between micellar and lamellar/vesicle regions, exhibiting intermediate rheological behavior. For the simulation section, a DPD model is established for OA and CPCI molecules and its validity is

separately confirmed based on reported self-assembly behavior of each component in water at different concentrations. Then DPD simulations of the structural change in CPCI surfactant aggregates are presented upon increasing the OA content of the ternary system. The simulation results show that mesophase formation in this system which occurs on the microsecond time scale in real systems follows the experimentally established equilibrium ternary phase diagram relatively well. Aggregate structures such as disk-like micelles, vesicles, and lamellar phases corresponding to the compositions in the ternary phase diagram are confirmed in simulations. With the decrease in water content along the OA/CPCI equimolar line, it was shown both in experiments and simulations that vesicles transition into lamellar structures. Upon increase in the OA content of the system, the micelle-to-lamellar transition is observed in both experiments and simulations along the constant CPCI concentration lines. Lastly, the effect of OA polarity on the final morphology of the ternary system is illustrated. The DPD method in this study validated by experiments can be an effective supplement for experimental setups and provides otherwise inaccessible mesoscopic information at the molecular level for a ternary phase of surfactant-polar oil-water. Apart from the scientific interest of such studies, the outcome highly affects the practical applications of surfactant systems such as liquid-in-liquid 3D printing,<sup>28,29</sup> for instance, determining how rapidly and what kind of mesophase forms. The established ternary phase diagram along with the DPD model can be used to predict and control the formation of structures like lamellar or vesicles, which can be used as simple model systems for biological membranes in life sciences applications.<sup>33</sup>

## Conflicts of interest

There are no conflicts to declare.

## Acknowledgements

Z.N. was supported by start-up funds from University of Missouri-Kansas City. R.J.H acknowledges funding from the National Science Foundation (NSF), the Division of Materials Research Polymers Program (CAREER proposal no: DMR-1942508). J.C.S. was supported by funding to the Blue Brain Project, a research center of the École polytechnique fédérale de Lausanne (EPFL), from the Swiss government's ETH Board of the Swiss Federal Institutes of Technology. We would like to thank Dr. Regine von Klitzing research group for fluorescence microscopy and Dr. Steffan Hardt research group for confocal microscopy at Technical University of Darmstadt. The authors are also grateful to Afnan Aladdad and Dr. Karl Kador for fluorescence microscopy at the University of Missouri–Kansas City (UMKC) School of Medicine.

## References

- 1 M. J. Rosen and J. T. Kunjappu, *Surfactants and Interfacial Phenomena*, Wiley, Hoboken, NJ, 2012.
- 2 J. N. Israelachvili, *Intermolecular and Surface Forces*, Academic Press, New York, 2011.
- 3 R. Strey, *Colloid Polym. Sci.*, 1994, **272**, 1005–1019.
- 4 M.-J. Schwuger, K. Stickdorn and R. Schomaecker, *Chem. Rev.*, 1995, **95**, 849–864.
- 5 F. S. Bates, W. W. Maurer, P. M. Lipic, M. A. Hillmyer, K. Almdal, K. Mortensen, G. H. Fredrickson and T. P. Lodge, *Phys. Rev. Lett.*, 1997, **79**, 849.
- 6 R. J. Hickey, T. M. Gillard, M. T. Irwin, D. C. Morse, T. P. Lodge and F. S. Bates, *Macromolecules*, 2016, **49**, 7928–7944.
- 7 R. J. Hickey, T. M. Gillard, M. T. Irwin, T. P. Lodge and F. S. Bates, *Soft Matter*, 2016, **12**, 53–66.
- 8 M. Kreilgaard, *Adv. Drug Deliv. Rev.*, 2002, **54**, S77–S98.
- 9 A. Kogan and N. Garti, *Adv. Colloid Interface Sci.*, 2006, **123**, 369–385.
- 10 J.-L. Salager, R. Antón, J. Bullón, A. Forgiarini and R. Marquez, *Cosmetics*, 2020, **7**, 57.
- 11 L. W. Lake, R. Johns, B. Rossen, G. A. Pope *et al.*, *Fundamentals of Enhanced Oil Recovery*, Society of Petroleum Engineers, Richardson, TX, 2014, vol. 1.
- 12 D. Levitt, A. Jackson, C. Heinson, L. N. Britton, T. Malik, V. Dwarakanath and G. A. Pope, SPE/DOE Symposium on Improved Oil Recovery, 2006.
- 13 J.-L. Salager, A. M. Forgiarini and J. Bullón, *J. Surfactants Deterg.*, 2013, **16**, 449–472.
- 14 M. Kahlweit, *Science*, 1988, **240**, 617–621.
- 15 B. K. Paul and S. P. Moulik, *Curr. Sci.*, 2001, 990–1001.
- 16 B. H. Jones and T. P. Lodge, *Polym. J.*, 2012, **44**, 131–146.
- 17 B. H. Jones and T. P. Lodge, *Chem. Mater.*, 2010, **22**, 1279–1281.
- 18 D. R. F. West and N. Saunders, *Ternary Phase Diagrams in Materials Science*, CRC Press, Boca Raton, FL, 2017.
- 19 J.-C. Zhao, *Methods for Phase Diagram Determination*, Elsevier, Amsterdam, 2011.
- 20 H. Li and J. Hao, *J. Phys. Chem. B*, 2008, **112**, 10497–10508.
- 21 T. Zemb, M. Dubois, B. Deme and T. Gulik-Krzywicki, *Science*, 1999, **283**, 816–819.
- 22 Y. A. Nastishin, *Langmuir*, 1996, **12**, 5011–5015.
- 23 J. Nakarapanich, T. Baramesangpet, S. Suksamranchit, A. Sirivat and A. Jamieson, *Colloid Polym. Sci.*, 2001, **279**, 671–677.
- 24 C. Noirjean, F. Testard, J. Jestin, O. Tache, C. Dejognat and D. Carriere, *Soft Matter*, 2014, **10**, 5928–5935.
- 25 T.-Q.-M. Tran, M.-F. Hsieh, K.-L. Chang, Q.-H. Pho, V.-C. Nguyen, C.-Y. Cheng, C.-M. Huang *et al.*, *Polymers*, 2016, **8**, 321.
- 26 A. P. Desbois and V. J. Smith, *Appl. Microbiol. Biotechnol.*, 2010, **85**, 1629–1642.
- 27 H. Morgan, D. M. Taylor and O. N. Oliveira Jr, *Biochim. Biophys. Acta - Biomembr.*, 1991, **1062**, 149–156.
- 28 H. Honaryar, J. A. LaNasa, E. C. Lloyd, R. J. Hickey and Z. Niroobakhsh, *Macromol. Rapid Commun.*, 2021, 2100445.
- 29 Z. Niroobakhsh, J. A. LaNasa, A. Belmonte and R. J. Hickey, *Phys. Rev. Lett.*, 2019, **122**, 178003.
- 30 I. Johansson and M. Svensson, *Curr. Opin. Colloid Interface Sci.*, 2001, **6**, 178–188.
- 31 M. Kjellin and I. Johansson, *Surfactants from Renewable*

- Resources, John Wiley & Sons, 2010.
- 32 C. Noirjean, F. Testard, C. Dejugnat, J. Jestin and D. Carriere, *Phys. Chem. Chem. Phys.*, 2016, **18**, 15911–15918.
- 33 A. Song, S. Dong, X. Jia, J. Hao, W. Liu and T. Liu, *Angew. Chem.*, 2005, **117**, 4086–4089.
- 34 D. Zhao, H. Li, A. Song and J. Hao, *Chin. Sci. bull.*, 2009, **54**, 3953–3957.
- 35 J. Hao and H. Hoffmann, *Curr. Opin. Colloid Interface Sci.*, 2004, **9**, 279–293.
- 36 P. Warren, P. Prinsen and M. Michels, *Philos. Trans. R. Soc. A*, 2003, **361**, 665–676.
- 37 J. C. Shelley and M. Y. Shelley, *Curr. Opin. Colloid Interface Sci.*, 2000, **5**, 101–110.
- 38 B. Smit, P. Hilbers and K. Esselink, *Int. J. Mod. Phys. C*, 1993, **4**, 393–400.
- 39 R. D. Groot and P. B. Warren, *J. Chem. Phys.*, 1997, **107**, 4423–4435.
- 40 J. Shillcock, M. Brochut, E. Chénais and J. Ipsen, *Soft Matter*, 2020, **16**, 6413–6423.
- 41 J. C. Shillcock, *Langmuir*, 2012, **28**, 541–547.
- 42 J. C. Shillcock and R. Lipowsky, *J. Chem. Phys.*, 2002, **117**, 5048–5061.
- 43 S. J. Marrink, V. Corradi, P. C. Souza, H. I. Ingolfsson, D. P. Tieleman and M. S. Sansom, *Chem. Rev.*, 2019, **119**, 6184–6226.
- 44 L. Gao, J. Shillcock and R. Lipowsky, *J. Chem. Phys.*, 2007, **126**, 01B602.
- 45 P. Prinsen, P. Warren and M. Michels, *Phys. Rev. Lett.*, 2002, **89**, 148302.
- 46 J. Padding and W. J. Briels, *J. Condens. Matter Phys.*, 2011, **23**, 233101.
- 47 J. Huang, M. Luo and Y. Wang, *J. Phys. Chem. B*, 2008, **112**, 6735–6741.
- 48 D. S. Bolintineanu, G. S. Grest, J. B. Lechman, F. Pierce, S. J. Plimpton and P. R. Schunk, *Comput. Part. Mech.*, 2014, **1**, 321–356.
- 49 R. Lipowsky, M. Brinkmann, R. Dimova, C. Haluska, J. Kierfeld and J. Shillcock, *J. Condens. Matter Phys.*, 2005, **17**, S2885.
- 50 M. Laradji and P. S. Kumar, *Phys. Rev. Lett.*, 2004, **93**, 198105.
- 51 I. Molinero, M. L. Sierra and E. Rodenas, *J. Colloid Interface Sci.*, 1997, **188**, 239–242.
- 52 Y. Michina, D. Carrière, C. Mariet, M. Moskura, P. Berthault, L. Belloni and T. Zemb, *Langmuir*, 2009, **25**, 698–706.
- 53 A. S. Yoshimura and R. K. Prud'homme, *J. Rheol.*, 1988, **32**, 575–584.
- 54 V. Bertola, F. Bertrand, H. Tabuteau, D. Bonn and P. Coussot, *J. Rheol.*, 2003, **47**, 1211–1226.
- 55 J. C. Shillcock, *Open Source Polymer Research Engine - Dissipative Particle Dynamics*, <https://github.com/Osprey-DPD/osprey-dpd>.
- 56 P. Espanol and P. B. Warren, *J. Chem. Phys.*, 2017, **146**, 150901.
- 57 R. D. Groot and K. Rabone, *Biophys. J.*, 2001, **81**, 725–736.
- 58 T. L. Rodgers, O. Mihailova and F. R. Siperstein, *J. Phys. Chem. B*, 2011, **115**, 10218–10227.
- 59 U. Ayachit, *The Paraview Guide: a Parallel Visualization Application*, Kitware, Inc., New York, NY, 2015.
- 60 J. Bhattacharjee, V. Aswal, P. Hassan, R. Pamu, J. Narayanan and J. Bellare, *Soft Matter*, 2012, **8**, 10130–10140.
- 61 D. Varade, T. Joshi, V. Aswal, P. Goyal, P. Hassan and P. Bahadur, *Colloids Surf. A Physicochem. Eng. Asp.*, 2005, **259**, 95–101.
- 62 E. W. Kaler, K. L. Herrington, A. K. Murthy and J. A. Zasadzinski, *The Journal of Physical Chemistry*, 1992, **96**, 6698–6707.
- 63 K. Horbaschek, H. Hoffmann and J. Hao, *J. Phys. Chem. B*, 2000, **104**, 2781–2784.
- 64 H. A. Barnes, J. F. Hutton and K. Walters, *An Introduction to Rheology*, Elsevier, Amsterdam, 1989, vol. 3.
- 65 Z. Niroobakhsh and A. Belmonte, *J. Non-Newton. Fluid Mech.*, 2018, **261**, 111–122.
- 66 M. Berni, C. Lawrence and D. Machin, *Adv. Colloid Interface Sci.*, 2002, **98**, 217–243.
- 67 B. Kronberg, K. Holmberg and B. Lindman, *Surface Chemistry of Surfactants and Polymers*, Wiley, Hoboken, NJ, 2014.
- 68 N. L. Sitnikova, R. Sprik, G. Wegdam and E. Eiser, *Langmuir*, 2005, **21**, 7083–7089.
- 69 S.-L. Yuan, Z.-T. Cai, G.-Y. Xu and Y.-S. Jiang, *Chem. Phys. Lett.*, 2002, **365**, 347–353.
- 70 B. Duan, X. Zhang, B. Qiao, B. Kong and X. Yang, *J. Phys. Chem. B*, 2009, **113**, 8854–8859.
- 71 I. Langmuir, *J. Am. Chem. Soc.*, 1917, **39**, 1848–1906.
- 72 J. Haldar, V. K. Aswal, P. S. Goyal and S. Bhattacharya, *J. Phys. Chem. B*, 2004, **108**, 11406–11411.
- 73 M. Seno, Y. Shiraishi, S. Takeuchi and J. Otsuki, *J. Phys. Chem.*, 1990, **94**, 3776–3780.
- 74 J. Mata, D. Varade, G. Ghosh and P. Bahadur, *Colloids Surf. A Physicochem. Eng. Asp.*, 2004, **245**, 69–73.
- 75 J. J. Janke, W. D. Bennett and D. P. Tieleman, *Langmuir*, 2014, **30**, 10661–10667.
- 76 K. Morigaki and P. Walde, *Curr. Opin. Colloid Interface Sci.*, 2007, **12**, 75–80.
- 77 D. P. Cistola, J. A. Hamilton, D. Jackson and D. M. Small, *Biochemistry*, 1988, **27**, 1881–1888.
- 78 Z. Niroobakhsh, M. Litman and A. Belmonte, *Phys. Rev. E.*, 2017, **96**, 053102.
- 79 W. D. Bennett, A. W. Chen, S. Donnini, G. Groenhof and D. P. Tieleman, *Can. J. Chem.*, 2013, **91**, 839–846.
- 80 A.-L. Fameau and T. Zemb, *Adv. Colloid Interface Sci.*, 2014, **207**, 43–64.
- 81 G. Pérez-Sánchez, J. R. Gomes and M. Jorge, *Langmuir*, 2013, **29**, 2387–2396.
- 82 V. A. Ngo, R. K. Kalia, A. Nakano and P. Vashishta, *J. Phys. Chem. B*, 2012, **116**, 13416–13423.
- 83 A. A. Gavrilov, Y. V. Kudryavtsev and A. V. Chertovich, *J. Chem. Phys.*, 2013, **139**, 224901.

- 84 R. Zana, *Adv. Colloid Interface Sci.*, 1995, **57**, 1–64.
- 85 B. Jonsson and H. Wennerstroem, *J. Phys. Chem.*, 1987, **91**, 338–352.
- 86 L. Chiappisi, H. Yalcinkaya, V. K. Gopalakrishnan, M. Gradzielski and T. Zemb, *Colloid Polym. Sci.*, 2015, **293**, 3131–3143.
- 87 P. Koshy, V. Aswal, M. Venkatesh and P. Hassan, *Soft Matter*, 2011, **7**, 4778–4786.
- 88 T. Zemb, D. Carrière, K. Glinel, M. Hartman, A. Meister, C. Vautrin, N. Delorme, A. Fery and M. Dubois, *Colloids Surf. A Physicochem. Eng. Asp.*, 2007, **303**, 37–45.